Use of eddy viscosity in resolvent analysis of turbulent channel flow

Sean Symon [*]

Aerodynamics and Flight Mechanics, Faculty of Engineering and Physical Sciences,
University of Southampton, Southampton SO17 1BJ, United Kingdom

Anagha Madhusudanan

Department of Applied Mathematics and Theoretical Physics, Centre for Mathematical Sciences,
University of Cambridge, Cambridge CB3 0WA, United Kingdom

Simon J. Illingworth and Ivan Marusic

Department of Mechanical Engineering, University of Melbourne, Parkville, Victoria 3010, Australia

The predictions obtained from resolvent analysis with and without an eddy viscosity model for turbulent channel flow at $\mathrm{Re}_\tau = 550$ are compared to direct numerical simulation data to identify the scales and wave speeds for which resolvent analysis provides good predictions. The low-rank behavior of the standard resolvent identifies energetic regions of the flow whereas the eddy resolvent is low rank when the resulting projection of the leading eddy resolvent mode onto the leading mode from spectral proper orthogonal decomposition is maximum. The highest projections are obtained for structures that are associated with the near-wall cycle and structures that are energetic at $z = \pm 0.5$. It is argued that these types of structures are likely to be correctly predicted for any friction Reynolds number due to the inner and outer scaling of the Cess eddy viscosity profile. The eddy resolvent also correctly identifies the most energetic wave speed for these two scales. For all other scales, neither analysis reliably predicts the most energetic wave speed or mode shapes. The standard resolvent tends to overestimate the most energetic wave speed while the eddy resolvent underestimates it. The resulting eddy resolvent modes are overly "attached" to the wall since the wall-normal gradient of the eddy viscosity overestimates the transport of energy towards the wall. These observations have direct implications for future work towards estimating turbulent channel flows using resolvent analysis and suggest that the Cess profile can be further optimized for individual scales to provide better low-order models of turbulent channel flows.

I. INTRODUCTION

The Navier-Stokes equations linearized around the mean (time-averaged) flow have been used to identify coherent structures in a variety of flows. In the resolvent-based approach of Ref. [1], for example, the linearized Navier-Stokes equations are analyzed from an input-output perspective. The

---

[*]sean.symon@soton.ac.uk

input is made up of nonlinear perturbation terms that are treated as an intrinsic forcing to the linear resolvent operator and the output is the perturbation velocity field. In the context of wall-bounded flows, resolvent analysis has been exploited for a variety of applications from finding reduced-order models of exact coherent states [2] to predicting statistics of high-Reynolds-number turbulence [3,4]. The ability of resolvent analysis to identify prominent linear mechanisms, moreover, has made it an attractive alternative to direct numerical simulation (DNS) for designing flow control strategies [5–7].

From DNS and experimental studies of wall-bounded flows, it is known that the production of turbulent kinetic energy is mainly driven by the exchange of energy from the mean flow to the fluctuations. Resolvent analysis models well this exchange from the mean to the fluctuations, where the mean is assumed to be known *a priori*. Therefore, the term in the energy budget that the resolvent analysis captures most successfully is production [8,9]. The resolvent operator also tends to be low rank for energy-producing scales [3]. The term that resolvent analysis captures the least accurately for an arbitrary scale is nonlinear transfer between scales. One way to model this term is to add an eddy viscosity to the resolvent operator [10–16]. The eddy viscosity provides additional dissipation that removes energy from all scales. As such, it attempts to model this nonlinear transfer of energy from the large scales to the small scales.

In terms of structures, many studies have observed good agreement between the structures predicted by resolvent analysis and those found in DNS. The leading resolvent mode, which is computed as the leading left singular vector of the resolvent operator, is the dominant structure predicted by resolvent analysis. The dominant mode from DNS is computed as the leading mode from spectral proper orthogonal decomposition (SPOD) [17,18]. In fact, if the nonlinear forcing is white in space and time, then resolvent and SPOD modes are theoretically equivalent [19]. The nonlinear forcing, however, is not white in space and time [15,20,21]. As such, the role of eddy viscosity is to model the effect of the nonlinear forcing such that white in space and time forcing is sufficient to predict the correct structures. Reference [13] showed that adding eddy viscosity improved predictions of coherent motions in turbulent channel flow at a friction Reynolds number of $Re_\tau = 1007$ and Ref. [22] compared resolvent predictions with and without eddy viscosity for turbulent channel flow at $Re_\tau = 2003$. The most comprehensive comparison between resolvent and SPOD modes was presented by Abreu *et al.* [23], who computed the projection of the leading resolvent mode onto the leading SPOD mode for turbulent pipe flow at low Reynolds numbers. The authors noted good agreement, i.e., high projections between the resolvent and SPOD modes, for scales where the lift-up mechanism [24,25] was active. A similar analysis was performed in Ref. [26] for turbulent channel flow using resolvent analysis with a number of eddy viscosity models.

The principal aim of this study is to identify the scales and wave speeds for which resolvent analysis with eddy viscosity provides good predictions and thereby also identify the scales that are not modeled accurately by the eddy resolvent. The predictions are quantified by calculating the projections of the leading resolvent mode with and without eddy viscosity onto the leading SPOD mode. The role of the wave speed in particular is analyzed since the energy of a structure is concentrated at the wall-normal location where its wave speed matches the local mean velocity. The inner and outer scalings of the Cess eddy viscosity profile provide additional evidence that structures which are energetic in the buffer and wake regions are predicted well by resolvent analysis with eddy viscosity. However, even at this relatively low Reynolds number of $Re_\tau = 550$, the structures which are energetic in the logarithmic regions are not predicted well by the eddy resolvent. This trend will likely worsen for higher Reynolds numbers, where the significance of structures in the log-layer increases. To explain these trends, we investigate the energy transfers introduced by eddy viscosity. Even though eddy viscosity adds extra dissipation to the energy balance, its wall-normal gradient transports energy towards the wall. The wall-normal profiles of the transfers introduced by eddy viscosity are examined to explain why resolvent modes for logarithmic structures are overly energetic near the wall. Although the eddy viscosity gradient biases resolvent modes of logarithmic structures towards the wall, it can potentially model local positive energy transfer in the near-wall region, which has been observed in DNS [27–30]. In other words, the success of resolvent analysis

with eddy viscosity depends on its ability to correctly model the wall-normal profile of nonlinear transfer.

The rest of the paper is organized as follows. Section II presents the governing equations for channel flow and provides a brief overview of resolvent analysis, the Cess eddy viscosity profile, and SPOD. The details of the DNS for $\mathrm{Re}_\tau = 550$ are provided in Sec. III. The predictions of resolvent and eddy analysis are evaluated in Sec. IV using scalar quantities. Section V provides a more detailed comparison of the mode shapes for select scales. The extent to which a constant eddy viscosity profile, i.e., one that does not depend on space, can successfully predict structures is also investigated in Sec. V. The energy transfer processes introduced by eddy viscosity are discussed in Sec. VI. The role of the eddy viscosity gradient, in particular, is examined and artificially manipulated to understand its influence on the mode shapes. Finally, conclusions and implications for optimizing a scale-dependent eddy viscosity are suggested in Sec. VII.

II. METHODOLOGY

Section II A describes the governing equations for plane Poiseuille flow and their nondimensionalization. A brief overview of resolvent analysis is provided in Sec. II B. In Sec. II C, a modified resolvent operator, which includes the Cess eddy viscosity profile, is formulated. In order to assess the predictive capability of resolvent analysis with and without eddy viscosity, the leading modes are compared to SPOD modes, which are computed using the procedure summarized in Sec. II D.

A. Plane Poiseuille flow equations

The nondimensional Navier-Stokes equations for statistically steady, turbulent plane Poiseuille flow are

$$\frac{\partial \boldsymbol{u}}{\partial t} + \boldsymbol{u} \cdot \nabla \boldsymbol{u} = -\nabla p + \frac{1}{\mathrm{Re}_\tau} \nabla^2 \boldsymbol{u}, \tag{1a}$$

$$\nabla \cdot \boldsymbol{u} = 0, \tag{1b}$$

where $\boldsymbol{u}(\boldsymbol{x}, t) = [u, v, w]^T$ is the velocity in the x (streamwise), y (spanwise), and z (wall-normal) directions, $p(\boldsymbol{x}, t)$ is the pressure, and $\nabla = [\partial/\partial x, \partial/\partial y, \partial/\partial z]^T$. The friction Reynolds number $\mathrm{Re}_\tau = u_\tau h / \nu$ is defined in terms of the friction velocity u_τ, channel half height h, and kinematic viscosity ν. Periodic boundary conditions are applied in the streamwise and spanwise directions and no-slip boundary conditions are imposed at the walls. The velocities are nondimensionalized by u_τ, the spatial variables by h, and the pressure by ρu_τ^2 where ρ is the density of the fluid. A "+" superscript denotes spatial variables that have been normalized by the viscous length scale ν/u_τ.

B. Resolvent analysis

Equation (1) is Reynolds decomposed, leading to the following equations for the fluctuations:

$$\frac{\partial \boldsymbol{u}'}{\partial t} + \boldsymbol{U} \cdot \nabla \boldsymbol{u}' + \boldsymbol{u}' \cdot \nabla \boldsymbol{U} + \nabla p' - \frac{1}{\mathrm{Re}_\tau} \nabla^2 \boldsymbol{u}' = -\boldsymbol{u}' \cdot \nabla \boldsymbol{u}' + \overline{\boldsymbol{u}' \cdot \nabla \boldsymbol{u}'} = \boldsymbol{f}', \tag{2a}$$

$$\nabla \cdot \boldsymbol{u}' = 0, \tag{2b}$$

where $(\bar{\cdot})$ and $(\cdot)'$ denote a time average and fluctuation, respectively. The mean velocity profile $\boldsymbol{U} = [U(z), 0, 0]^T$ is assumed to be known *a priori* from DNS. Equation (2) is written such that all linear terms appear on the left-hand side. The nonlinear terms on the right-hand side are lumped together as a forcing $\boldsymbol{f}'$. Equation (2) is Laplace transformed in time and Fourier transformed in the homogeneous directions x and y:

$$\hat{\boldsymbol{u}}(k_x, k_y, s) = \frac{1}{(2\pi)^3} \int_{-\infty}^{\infty} \int_{-\infty}^{\infty} \int_{-\infty}^{\infty} \boldsymbol{u}'(x, y, z, t) e^{st - ik_x x - ik_y y} dx \, dy \, dt. \tag{3}$$

Upon integration of Eq. (3), we set $s = i\omega$ to consider the frequency response $\hat{u}(\mathbf{k})$ where $(\hat{\cdot})$ denotes the Fourier-transformed coefficient and the wavenumber triplet $\mathbf{k} = (k_x, k_y, \omega)$ consists of streamwise wavenumber k_x, spanwise wavenumber k_y, and temporal frequency ω. The equivalent wavelengths in the streamwise and spanwise directions are $\lambda_x = 2\pi/k_x$ and $\lambda_y = 2\pi/k_y$. The wavenumbers are nondimensionalized by $(1/h)$ and the wavelengths by h.

Equation (3) is substituted into Eq. (2) and rearranged into state-space form [31],

$$i\omega\hat{\mathbf{q}}(\mathbf{k}) = \mathbf{A}(k_x, k_y)\hat{\mathbf{q}}(\mathbf{k}) + \mathbf{B}(k_x, k_y)\hat{\mathbf{f}}(\mathbf{k}), \tag{4a}$$

$$\hat{\mathbf{u}}(\mathbf{k}) = \mathbf{C}(k_x, k_y)\hat{\mathbf{q}}(\mathbf{k}), \tag{4b}$$

where the state $\hat{\mathbf{q}}$ consists of the wall-normal velocity $\hat{w}$ and wall-normal vorticity $\hat{\eta} = ik_y\hat{u} - ik_x\hat{v}$. The matrices $\mathbf{A}$, $\mathbf{B}$, and $\mathbf{C}$ are the discretized forms of the linearized Navier-Stokes operator, the forcing operator, and the output operator, respectively. The expressions for the matrices $\mathbf{A}$, $\mathbf{B}$, and $\mathbf{C}$ are given in Appendix A. The operators are discretized numerically with $N_y = 201$ Chebyshev collocation points and the discretized differentiation operators are formed using the suite developed in Ref. [32]. The convergence of the results is ensured by checking that they are not modified when the number of collocation points is doubled. It is worth noting that $\mathbf{A}$, $\mathbf{B}$, and $\mathbf{C}$ are independent of ω but are functions of the wavenumber pair (k_x, k_y) under consideration. For the sake of brevity, this dependence is omitted for the rest of the paper.

Equation (4) is recast into input-output form,

$$\hat{\mathbf{u}}(\mathbf{k}) = \mathbf{C}(i\omega\mathbf{I} - \mathbf{A})^{-1}\hat{\mathbf{f}}(\mathbf{k}) = \mathcal{H}(\mathbf{k})\hat{\mathbf{f}}(\mathbf{k}), \tag{5}$$

where $\mathcal{H}(\mathbf{k})$ is a linear operator called the resolvent that relates the input forcing $\hat{\mathbf{f}}(\mathbf{k})$ to the output velocity $\hat{\mathbf{u}}(\mathbf{k})$. Even if $\hat{\mathbf{f}}(\mathbf{k})$ is unknown, the resolvent operator can be characterized by the singular value decomposition

$$\mathcal{H}(\mathbf{k}) = \hat{\boldsymbol{\Psi}}(\mathbf{k})\boldsymbol{\Sigma}(\mathbf{k})\hat{\boldsymbol{\Phi}}^*(\mathbf{k}), \tag{6}$$

where $\hat{\boldsymbol{\Psi}}(\mathbf{k}) = [\hat{\boldsymbol{\psi}}_1(\mathbf{k}), \hat{\boldsymbol{\psi}}_2(\mathbf{k}), \ldots, \hat{\boldsymbol{\psi}}_p(\mathbf{k})]$ are the resolvent modes, which form an orthogonal basis for velocity, and $\hat{\boldsymbol{\Phi}}(\mathbf{k}) = [\hat{\boldsymbol{\phi}}_1(\mathbf{k}), \hat{\boldsymbol{\phi}}_2(\mathbf{k}), \ldots, \hat{\boldsymbol{\phi}}_p(\mathbf{k})]$ are the resolvent forcing modes which form an orthogonal basis for the nonlinear forcing. $\boldsymbol{\Sigma}(\mathbf{k})$ is a diagonal matrix that ranks the pth structure by its gain $\sigma_p(\mathbf{k})$ using an inner product that is proportional to its kinetic energy, i.e., $\langle \hat{\boldsymbol{\psi}}, \hat{\boldsymbol{\psi}} \rangle = \int_{-h}^{h} \hat{\boldsymbol{\psi}}^* \cdot \hat{\boldsymbol{\psi}} dz$. The structure $\hat{\boldsymbol{\psi}}_1(\mathbf{k})$ is, therefore, referred to as the optimal or leading resolvent mode and is the most amplified response of the linear dynamics contained in the resolvent.

The true velocity field from experiments or DNS can be expressed as a weighted sum of resolvent modes,

$$\hat{\mathbf{u}}(\mathbf{k}) = \sum_{p=1}^{N} \hat{\boldsymbol{\psi}}_p(\mathbf{k})\sigma_p(\mathbf{k})\chi_p(\mathbf{k}), \tag{7}$$

where $\chi_p(\mathbf{k})$ is the projection of $\hat{\boldsymbol{\phi}}_p(\mathbf{k})$ onto $\hat{\mathbf{f}}(\mathbf{k})$, i.e.,

$$\chi_p(\mathbf{k}) = \langle \hat{\mathbf{f}}(\mathbf{k}), \hat{\boldsymbol{\phi}}_p(\mathbf{k}) \rangle. \tag{8}$$

It can be noted from Eqs. (7) and (8) that if $\hat{\mathbf{f}}(\mathbf{k})$ is white noise or projects equally onto the resolvent forcing modes, then the contribution of a resolvent mode $\hat{\boldsymbol{\psi}}_p$ in reconstructing the velocity field according to Eq. (7) is solely dependent on the associated singular value σ_p. Moreover, if $\sigma_1 \gg \sigma_2$, then it is often argued that the velocity response can be well approximated by the leading resolvent response mode $\hat{\boldsymbol{\psi}}_1$ alone.

C. Cess eddy viscosity model

It has been shown, however, that the nonlinear forcing may have little to no overlap with the leading forcing mode [8,15,33] resulting in $\chi_1 \ll \chi_{p\neq1}$. This nonalignment stems from the fact that

the resolvent does not model well the interscale nonlinear transfer. To address this shortcoming, an eddy viscosity can be added to the linearized Navier-Stokes equations after performing a triple decomposition of the total velocity field $\tilde{\boldsymbol{u}}$ into a mean component $\boldsymbol{U}$, coherent motions $\boldsymbol{u}$, and incoherent fluctuations $\boldsymbol{u}'$ [10]. A new set of equations govern the coherent velocity and pressure:

$$\frac{\partial \boldsymbol{u}}{\partial t} + \boldsymbol{U} \cdot \nabla \boldsymbol{u} + \boldsymbol{u} \cdot \nabla \boldsymbol{U} + \nabla p - \frac{1}{\mathrm{Re}_\tau} \nabla \cdot \left[\frac{\nu_T}{\nu} (\nabla \boldsymbol{u} + \nabla \boldsymbol{u}^T) \right] = \boldsymbol{d}, \tag{9}$$

where $\nu_T(z)$ is the total effective viscosity and $\boldsymbol{d} = -\boldsymbol{u} \cdot \nabla \boldsymbol{u} + \overline{\boldsymbol{u} \cdot \nabla \boldsymbol{u}}$ is the disturbance term. Similar to Refs. [34] and [12], the Cess [35] eddy viscosity profile,

$$\nu_T(z) = \frac{\nu}{2} \left[1 + \frac{\kappa^2 \mathrm{Re}_\tau^2}{9} (1 - z^2)^2 (1 + 2z^2)^2 \left(1 - \exp\left[(|z| - 1) \frac{\mathrm{Re}_\tau}{A} \right] \right)^2 \right]^{1/2} + \frac{\nu}{2}, \tag{10}$$

is employed in this study. The constants $\kappa = 0.426$ and $A = 25.4$ are chosen based on a least-squares fit to experimental mean velocity profiles at $\mathrm{Re}_\tau = 2000$ [36]. Even though the Reynolds number in this study is lower than the Reynolds number for which the fit was performed, it has been verified that the results are not sensitive to the values of these constants. Appendix B, moreover, illustrates that eddy viscosity profiles computed directly from the DNS mean velocity profile yield nearly identical results to the Cess profile in Eq. (10).

As done in Sec. II B, Eq. (9) is Fourier transformed in time and the homogeneous directions to obtain an input-output relationship between the velocity and disturbance fields,

$$\hat{\boldsymbol{u}}(\boldsymbol{k}) = \mathcal{H}^e(\boldsymbol{k}) \hat{\boldsymbol{d}}(\boldsymbol{k}), \tag{11}$$

where $\mathcal{H}^e(\boldsymbol{k})$ is a modified resolvent operator henceforth referred to as the eddy resolvent. Its singular value decomposition can be written as

$$\mathcal{H}^e(\boldsymbol{k}) = \hat{\boldsymbol{\Psi}}^e(\boldsymbol{k}) \boldsymbol{\Sigma}^e(\boldsymbol{k}) \hat{\boldsymbol{\Phi}}^{*,e}(\boldsymbol{k}). \tag{12}$$

The superscript e differentiates the eddy resolvent modes, henceforth referred to as eddy modes, and singular values from their standard resolvent counterparts in Eq. (6). The interpretation of each term in the decomposition is similar to Eq. (6) in that $\hat{\Psi}^e(\boldsymbol{k})$ consists of orthogonal basis functions for the velocity field and the diagonal matrix $\boldsymbol{\Sigma}^e(\boldsymbol{k})$ ranks the pth structure by its gain using an inner product proportional to its kinetic energy. The matrix $\hat{\Phi}^e(\boldsymbol{k})$, on the other hand, contains orthogonal basis functions for the disturbance field $\hat{\boldsymbol{d}}(\boldsymbol{k})$ which is less interpretable than $\hat{\boldsymbol{f}}(\boldsymbol{k})$. Despite this drawback, the addition of eddy viscosity is expected to partially model the effect of $\hat{\boldsymbol{f}}(\boldsymbol{k})$ and thus improve the efficiency of eddy modes as a basis for the velocity field.

D. Spectral proper orthogonal decomposition

The efficiency of resolvent and eddy modes as a basis for the velocity field can be assessed by projecting them onto SPOD modes, which are computed directly from data. The SPOD modes are computed with the same procedure described in Ref. [19] so only a brief summary is presented here. Using Welch's method [37], the DNS data for a particular (k_x, k_y) are divided into overlapping segments containing 512 snapshots with 75% overlap. Each segment is Fourier transformed in time and the Fourier modes for a specific frequency ω can be arranged into the new data matrix

$$\hat{\boldsymbol{Q}}(\boldsymbol{k}) = \begin{bmatrix} \hat{\boldsymbol{q}}_\omega^{(1)} & \hat{\boldsymbol{q}}_\omega^{(2)} & \cdots & \hat{\boldsymbol{q}}_\omega^{(s)} \end{bmatrix} \in \mathbb{C}^{m \times s}, \tag{13}$$

where m represents the number of states and s the number of segments. The cross-spectral density matrix for a specific wavenumber triplet $\hat{\boldsymbol{S}}(\boldsymbol{k})$ is

$$\hat{\boldsymbol{S}}(\boldsymbol{k}) = \hat{\boldsymbol{Q}}(\boldsymbol{k}) \hat{\boldsymbol{Q}}^*(\boldsymbol{k}). \tag{14}$$

TABLE I. Channel flow DNS parameters.

Re_τ	L_x	L_y	L_z	N_x	N_y	N_z	Δx^+	Δy^+	$\Delta z^+_{\min}$	$\Delta z^+_{\max}$
550	2π	π	$2h$	256	256	201	13.5	6.75	6.79×10^{-2}	8.64

The SPOD eigenvectors (or modes) $\hat{V}(k)$ and eigenvalues $\Lambda(k)$ can be obtained by performing an eigenvalue decomposition of the cross-spectral density matrix,

$$\hat{S}(k)\hat{V}(k) = \hat{V}(k)\Lambda(k). \tag{15}$$

III. DNS DATASET

A DNS of channel flow at $Re_\tau = 550$ is performed using the CHANNELFLOW pseudospectral code [38]. Table I summarizes the parameters of the simulation which was solved on a domain with dimensions $2\pi \times \pi \times 2h$ in the streamwise (L_x), spanwise (L_y), and wall-normal (L_z) directions. There are $N_x = N_y = 256$ equally spaced points in the streamwise and spanwise directions and $N_y = 201$ points in the wall-normal direction on a Chebyshev grid. Periodic boundary conditions are employed in the streamwise and spanwise directions while no-slip boundary conditions are enforced on the channel walls. Further details on the mesh discretization (Δx^+, Δy^+, $\Delta z^+_{\min}$, $\Delta z^+_{\max}$) are presented in Table I. The mean velocity and Reynolds stress profiles are presented in Figs. 1(a) and 1(b), respectively. All profiles show good agreement with the DNS results from Ref. [39] despite the smaller computational box in this study.

SPOD is performed on a database of 6784 snapshots that have been used to generate Fig. 1. The time resolution is $\Delta t = 0.2$ and the data are divided into equal segments containing 512 snapshots with an overlap of 75% in order to obtain sufficient frequency resolution for $k_x = 1$ modes. There are 50 segments, which is comparable with many previous studies [13,15,21,40] and ensures that the leading pair of SPOD modes is converged. The cross-spectral density matrices in Eq. (14) are computed using Welch's method with a Hamming window. The SPOD modes and their respective energies for a desired frequency are obtained from the eigenvectors and eigenvalues, respectively, of the cross-spectral density matrices.
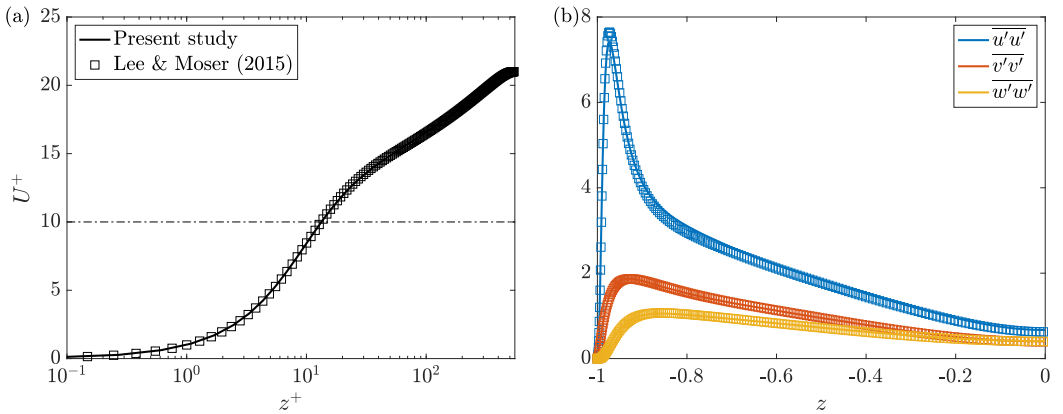

FIG. 1. (a) Mean velocity profile and (b) Reynolds stress profiles from the present study (solid lines) and Ref. [39] (open squares).
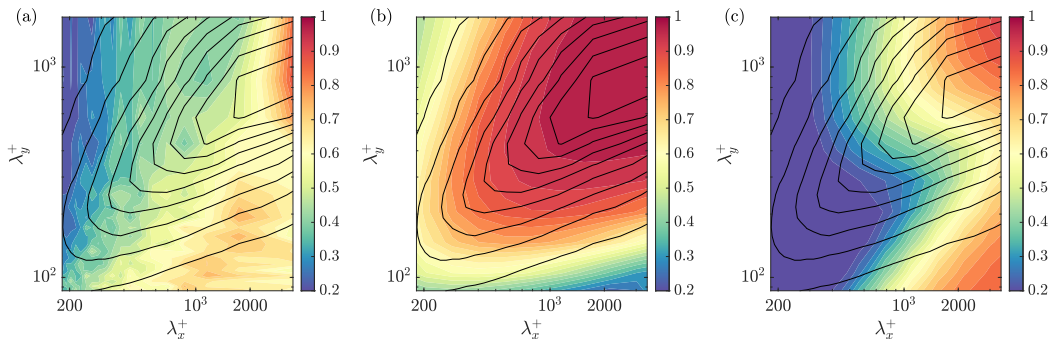
FIG. 2. Low-rank maps for (a) SPOD, (b) the standard resolvent, and (c) the eddy resolvent for a fixed wave speed of $c^+ = 18.9$. Contours of the turbulent kinetic energy spectrum at $z = -0.5$ are denoted in black.

IV. STANDARD AND EDDY RESOLVENT PREDICTIONS

In this section, the predictions from standard and eddy resolvent analysis are compared to DNS data using several measures. To begin with, the low-rank behavior of the SPOD modes (computed from the cross-spectral density matrix) is compared to those of the resolvent modes in Sec. IV A. Next, the projection of the dominant SPOD mode onto the leading resolvent and eddy modes is computed in Sec. IV B for the most energetic wavenumber pairs. Structures convecting at a range of wave speeds $c^+ = \omega/k_x$ are considered and projections are computed independently for each wave speed. In Sec. IV C, the wave speed of the most energetic SPOD mode is compared to the most amplified wave speed identified by standard and eddy resolvent analysis for a range of (k_x, k_y) wavenumber pairs. This motivates the selection of specific wavenumber triplets to examine in greater detail in Sec. V in which the SPOD, resolvent, and eddy mode shapes are compared directly.

A. Low-rank maps

An important aspect of the cross-spectral density matrix is its rank or, more specifically, the percentage of the total energy that is captured by the leading SPOD modes alone. Due to the symmetry of the channel, SPOD eigenvalues come in (approximately) equal pairs. One mode in each pair is symmetric with respect to the channel centerline while the other mode is antisymmetric. The low-rank behavior of SPOD modes can therefore be studied by computing the ratio of the dominant pair of eigenvalues to the sum of all eigenvalues:

$$\mathcal{R}(\boldsymbol{k}) = \frac{\lambda_1^2(\boldsymbol{k}) + \lambda_2^2(\boldsymbol{k})}{\sum_p \lambda_p^2(\boldsymbol{k})}. \tag{16}$$

The low-rank behavior of the SPOD modes can be compared to that of standard resolvent or eddy resolvent modes by using the singular values obtained from the resolvent analysis in Eq. (16) in place of the SPOD eigenvalues.

The low-rank maps are computed across $(\lambda_x^+, \lambda_y^+)$ for a fixed wave speed of $c^+ = 18.9$ and are shown for the case of DNS, standard resolvent, and eddy resolvent in Figs. 2(a), 2(b), and 2(c), respectively. Since Ref. [3] noted good agreement between the low-rank behavior of the standard resolvent and the turbulent kinetic energy spectrum, contours of the latter have been superimposed onto the low-rank maps in Fig. 2. Low-rank behavior for the SPOD modes is observed for high-aspect-ratio structures, i.e., $\lambda_x > \lambda_y$, in Fig. 2(a). The first pair of SPOD modes is dominant for the longest structures with a spanwise wavelength of $\lambda_y^+ \approx 10^3$. The SPOD modes are also low rank for structures clustered around $(\lambda_x^+, \lambda_y^+) = (1000, 100)$ although for the wave speed under

consideration these structures are not particularly energetic. There is less agreement, therefore, between the kinetic energy contours and the low-rank map for the SPOD modes.

The low-rank maps for the standard and eddy resolvents in Figs. 2(b) and 2(c), respectively, are remarkably different. The standard resolvent does not predict well the low-rank behavior of SPOD modes. In fact, the flow is generally of much higher rank than the predictions of the standard resolvent. There is, nonetheless, excellent agreement between the low-rank map of the standard resolvent and the turbulent kinetic energy spectrum. This suggests that the standard resolvent is good at identifying linear amplification mechanisms which translate into high energy production and, therefore, turbulent kinetic energy. The eddy resolvent, meanwhile, predicts well the low-rank behavior of the SPOD modes. Nonetheless, the eddy resolvent is of lower rank for structures with spanwise wavelengths of $\lambda_y^+ = 100$ than the SPOD modes.

It can be remarked that the addition of eddy viscosity significantly alters the linear mechanisms identified by the standard resolvent. Although not shown here for the sake of brevity, the eddy resolvent is low rank for spanwise wavelengths of $\lambda_y^+ = 80$ and $\lambda_y = 3.5$ regardless of the wave speed selected. As such, eddy analysis is less successful in identifying the energetic scales for a specified wave speed but can predict more accurately the rank of the SPOD modes. These results, notwithstanding, do not quantify the accuracy of resolvent or eddy analysis in predicting flow structures in turbulent channel flow. It will be seen that the two peak spanwise wavelengths identified by the eddy resolvent low-rank maps provide a valuable clue in identifying the types of structures that the eddy resolvent predicts with good accuracy.

B. Projection of resolvent modes onto SPOD modes

The objective of this section is to quantify the accuracy of standard and eddy resolvent analysis by projecting the leading SPOD mode $\hat{\boldsymbol{v}}_1(\boldsymbol{k})$ from DNS onto the leading resolvent $\hat{\boldsymbol{\psi}}_1(\boldsymbol{k})$ and eddy $\hat{\boldsymbol{\psi}}_1^e(\boldsymbol{k})$ modes. Similar analyses have been performed in Refs. [23] and [16] for turbulent pipe flow and turbulent jets, respectively. To account for the pairing of resolvent and eddy modes, the leading SPOD mode is projected onto both the first and second resolvent and/or eddy modes:

$$\gamma(\boldsymbol{k}) = \sqrt{\left(\frac{\langle \hat{\boldsymbol{v}}_1(\boldsymbol{k}), \hat{\boldsymbol{\psi}}_1(\boldsymbol{k})\rangle}{\|\hat{\boldsymbol{v}}_1(\boldsymbol{k})\| \cdot \|\hat{\boldsymbol{\psi}}_1(\boldsymbol{k})\|}\right)^2 + \left(\frac{\langle \hat{\boldsymbol{v}}_1(\boldsymbol{k}), \hat{\boldsymbol{\psi}}_2(\boldsymbol{k})\rangle}{\|\hat{\boldsymbol{v}}_1(\boldsymbol{k})\| \cdot \|\hat{\boldsymbol{\psi}}_2(\boldsymbol{k})\|}\right)^2}, \tag{17a}$$

$$\gamma^e(\boldsymbol{k}) = \sqrt{\left(\frac{\langle \hat{\boldsymbol{v}}_1(\boldsymbol{k}), \hat{\boldsymbol{\psi}}_1^e(\boldsymbol{k})\rangle}{\|\hat{\boldsymbol{v}}_1(\boldsymbol{k})\| \cdot \|\hat{\boldsymbol{\psi}}_1^e(\boldsymbol{k})\|}\right)^2 + \left(\frac{\langle \hat{\boldsymbol{v}}_1(\boldsymbol{k}), \hat{\boldsymbol{\psi}}_2^e(\boldsymbol{k})\rangle}{\|\hat{\boldsymbol{v}}_1(\boldsymbol{k})\| \cdot \|\hat{\boldsymbol{\psi}}_2^e(\boldsymbol{k})\|}\right)^2}. \tag{17b}$$

Both $\gamma(\boldsymbol{k})$ and $\gamma^e(\boldsymbol{k})$ have a maximum value of unity, which indicates perfect alignment between SPOD and resolvent and/or eddy modes. A value of zero indicates that the mode shapes are orthogonal. It should be noted that nearly identical results are obtained if γ and γ^e are computed using the second SPOD mode since the SPOD modes come in pairs. For the sake of brevity, these results have been omitted.

Figure 3 illustrates γ for $180 < \lambda_x^+ < 3400$ and $80 < \lambda_y^+ < 1700$. These scales contain most of the kinetic energy in the flow and include structures associated with the near-wall cycle. Streamwise-constant modes are discussed in greater detail in Sec. V. The colorbar in Fig. 3 is restricted to a range [0.5, 1] to facilitate identification of scales where there is significant overlap between the SPOD and resolvent modes. Each panel in Fig. 3 represents a different wave speed and contains contours of the turbulent kinetic energy spectrum at the wall-normal location where $U^+ = c^+$. The lowest wave speed considered is $c^+ = 10.3$ in Fig. 3(a) and c^+ increases at increments of approximately 1.7, culminating in a wave speed of $c^+ = 18.9$ in Fig. 3(f). The lower bound on c^+ is motivated by the near-wall streaks being most energetic at a wall-normal location of $z^+ = 15$ where $U^+ \approx 10$ [1].
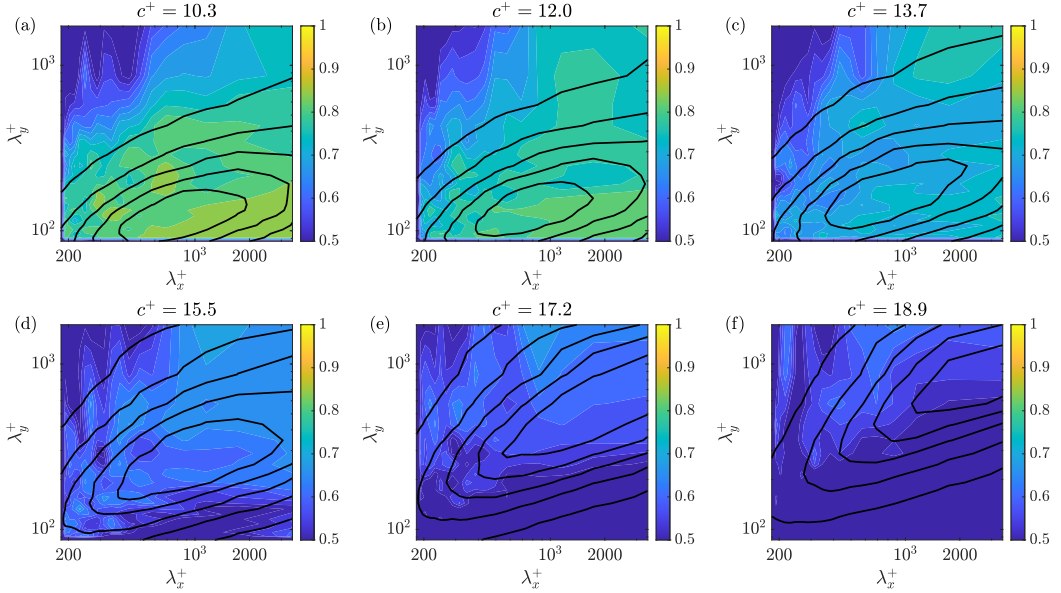
FIG. 3. Projection of the leading SPOD mode onto the leading pair of resolvent modes for various wave speeds. Contours of the turbulent kinetic energy spectrum at the wall-normal location where $c^+ = U^+$ are denoted in black.

The upper bound on c^+ is chosen since it is approximately $c^+ = U_{CL}^+ - 2$, which translates to a wall-normal location of $z = -0.5$.

Figure 3 shows that there is good agreement between the leading SPOD and resolvent modes for $c^+ = 10.3$. Despite some outliers, Fig. 3(a) indicates that the highest projections are for modes that satisfy $k_x < k_y$. This is consistent with the results of Ref. [23] which noted that the lift-up mechanism leads to large amplification for high-aspect-ratio scales where $/AR = k_y/k_x$. The scales that have high projection coefficients are approximately the same as those that are energetic at the wall-normal location where $c^+ = U^+ = 10.3$. As the wave speed increases, however, the values of γ decline quite significantly, indicating poorer predictions of the mode shapes from resolvent analysis. For the highest wave speed in Fig. 3(f), $\gamma < 0.5$ for most scales and the maximum values of γ do not coincide with the most energetic scales.

Figure 4 presents the projection coefficient for the eddy resolvent. There is significantly better agreement between the leading SPOD and eddy modes at all wave speeds in comparison to the standard resolvent in Fig. 3. There are, however, some similarities between γ and γ^e. First, the highest values of γ^e are obtained for high-aspect-ratio structures. Second, the wave speed has a major influence on γ^e. For $c^+ = 10.3$, the SPOD and eddy modes are in good agreement for scales associated with the near-wall streaks. As such, the scales for which $\gamma^e > 0.9$ coincide with the turbulent kinetic energy spectrum at $z^+ = 15$, i.e., the wall-normal location where $c^+ = U^+ = 10.3$. For the next four wave speeds in Figs. 4(b)–4(e), the SPOD and eddy modes are in good agreement for scales with large λ_x^+; however, these are not necessarily the most energetic scales at the corresponding wall-normal location. In Fig. 4(d), for example, the highest values of γ^e do not coincide with the maximum turbulent kinetic energy. For $c^+ = 18.9$ in Fig. 4(f), there is good agreement between high values of γ^e and the turbulent kinetic energy. One final observation is that there are two spanwise wavelengths for which high values of γ^e are observed at higher wave speeds: $\lambda_y^+ \approx 80$ and $\lambda_y \approx 3.5$. This is consistent with the SPOD and eddy resolvent low-rank maps in Fig. 2 and suggests that scales for which the eddy resolvent is low rank are scales for which eddy analysis predicts well the leading SPOD modes.
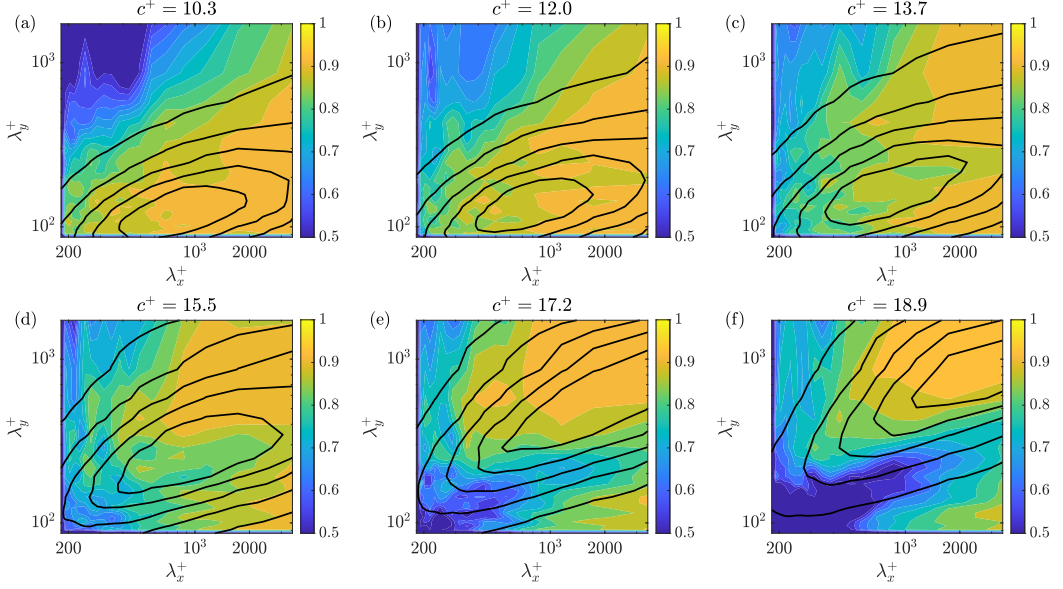
FIG. 4. Projection of the leading SPOD mode onto the leading pair of eddy modes for various wave speeds. Contours of the turbulent kinetic energy spectrum at the wall-normal location where $c^+ = U^+$ are denoted in black.

C. Frequency response

The previous sections show that there is a trade-off when eddy viscosity is added to the resolvent operator. On one hand, eddy viscosity distorts the linear dynamics of the operator such that the low-rank map resembles less the turbulent kinetic energy spectrum. On the other hand, the eddy modes have larger projections onto SPOD modes than their resolvent mode counterparts. Although these comparisons have been studied for a variety of wave speeds, the impact of eddy viscosity on the resolvent frequency response has yet to be analyzed. In order to be consistent with previous sections, the frequency response is considered from a wave speed point of view. The impact of eddy viscosity can be better appreciated by considering a single wavenumber pair initially before investigating all energetic wavenumber pairs as done in the previous sections. The wavenumber pair $(k_x, k_y) = (4, 30)$, which corresponds to $(\lambda_x^+, \lambda_y^+) = (864, 116)$, is selected as it corresponds to the near-wall streaks in the DNS used in this study.

To gain a better understanding of what the addition of eddy viscosity does to modify the frequency response of the resolvent operator, we look at a range of eddy-viscosity-based models, where the strength of the eddy viscosity is gradually increased from zero (equivalent to the standard resolvent) to the full eddy viscosity. The strength of the eddy viscosity is adjusted artificially by introducing the scaling factor $\mathcal{S}$ such that Eq. (10) becomes

$$\nu_T(z) = \frac{\nu}{2}\left[1 + \mathcal{S}\left\{\frac{\kappa^2 \mathrm{Re}_\tau^2}{9}(1 - z^2)^2(1 + 2z^2)^2\left(1 - \exp\left[(|z| - 1)\frac{\mathrm{Re}_\tau}{A}\right]\right)^2\right\}\right]^{1/2} + \frac{\nu}{2}, \quad (18)$$

where $\mathcal{S} \in [0, 1]$. Setting $\mathcal{S} = 0$ or $\mathcal{S} = 1$ is equivalent to standard resolvent or eddy resolvent analysis, respectively. A similar parameter was introduced in Ref. [41] to derive a scale-dependent eddy viscosity for linear estimation of a turbulent channel flow at $\mathrm{Re}_\tau = 2003$. The first singular value σ_1 is plotted against c^+ in Fig. 5 for various strengths of eddy viscosity, i.e., different values of $\mathcal{S}$. As the value of $\mathcal{S}$ increases, both the maximum amplification and the most amplified wave speed decrease. For this particular scale, moreover, the maximum amplification declines by a factor
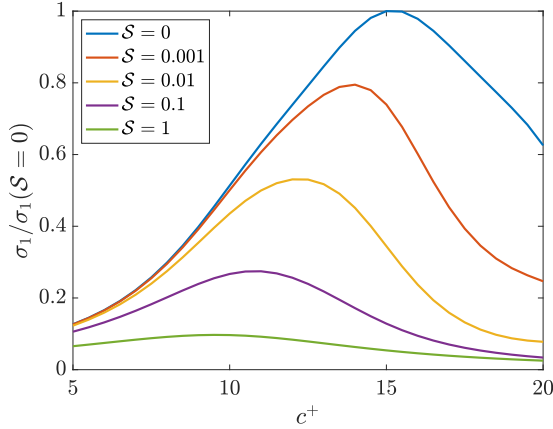
FIG. 5. Most energetic wave speed for $(k_x, k_y) = (4, 30)$ as a function of different strengths of the eddy viscosity as denoted by $\mathcal{S}$.

of 10 and the most amplified wave speed slows down substantially from $c^+ = 15.5$ to $c^+ = 9.5$. A crude explanation for this behavior is that the damping supplied by eddy viscosity results in slower, less amplified structures. Since standard resolvent analysis has absolutely no damping other than molecular viscosity, the structures are allowed to convect more quickly. It can, therefore, be expected that for an arbitrary scale the most amplified wave speed predicted by standard resolvent analysis is going to be greater than that predicted by eddy resolvent analysis.

This hypothesis is tested in Fig. 6, which compares the wave speed corresponding to the maximum λ_1 from DNS (SPOD) to the most amplified wave speed predicted by the standard and eddy resolvent for the most energetic wavenumber pairs (these will be referred to as the maximum wave speed). The only similarity among the three panels is that the maximum wave speed is primarily governed by the spanwise wavenumber. Wider structures, i.e., those with small spanwise wavenumbers, travel faster than relatively less wide structures. The streamwise wavenumber plays a bigger role in DNS and the standard resolvent than it does for the eddy resolvent. Figures 6(a) and 6(b) show that for fixed k_y, the maximum wave speed increases as a function of k_x. Thus, the trend for k_x is different from k_y in that longer structures, i.e., those with smaller k_x, travel slower, while wider structures, i.e., those with smaller k_y, travel faster. Another interpretation of these trends is that higher-aspect-ratio structures convect more slowly and are thus more energetic closer to the wall. Lower-aspect-ratio structures, meanwhile, convect more quickly and are thus more energetic
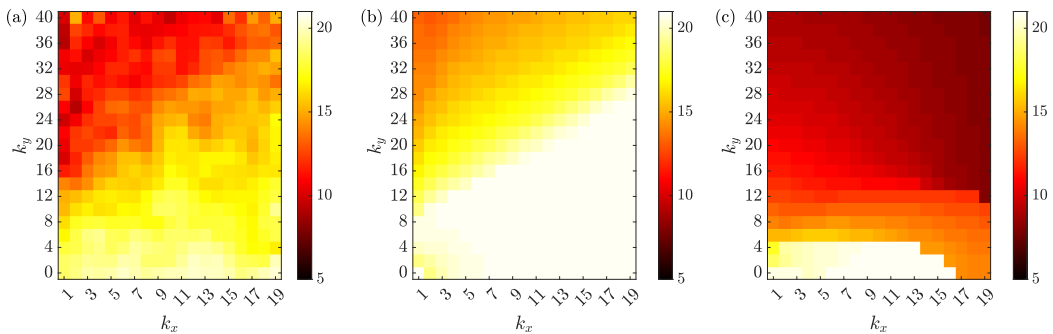

FIG. 6. Wave speed corresponding to the maximum λ_1 computed from (a) DNS compared to the most amplified wave speed predicted by the (b) standard resolvent and (c) eddy resolvent.
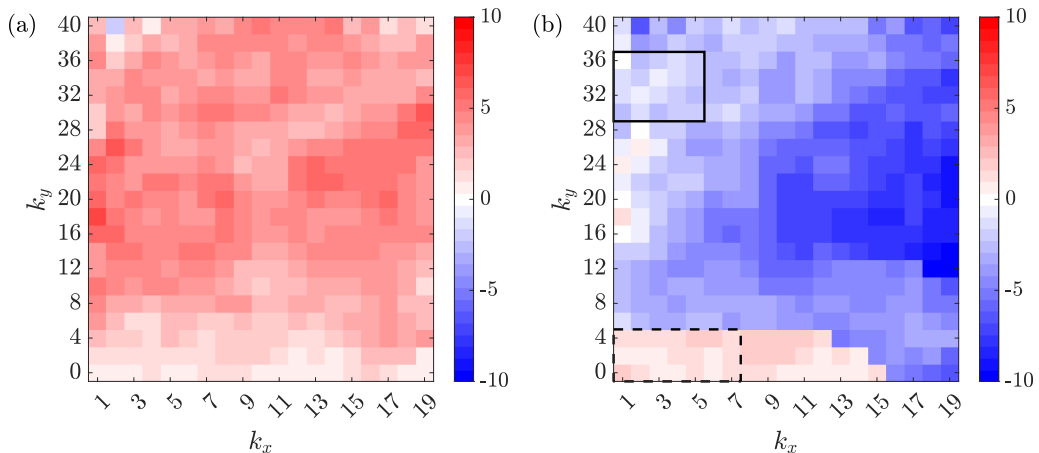
FIG. 7. Difference between the most amplified wave speed predicted by the (a) standard resolvent and (b) eddy resolvent compared to the wave speed corresponding to the maximum λ_1 computed from DNS.

away from the wall. These trends are consistent with observations from Ref. [42] among others who report aspect ratios of approximately $/AR = 8$ for near-wall coherent motions and $/AR = 2$–3 for large-scale outer motions.

Figure 7 plots the difference between the maximum wave speed predicted by the standard and eddy resolvents and that of DNS. Red squares indicate that the maximum wave speed is too high and blue squares that the maximum wave speed is too low. It is striking how large the differences are particularly for the relatively small Reynolds number considered in this study which restricts the range of wave speeds that can be expected in the flow. Figure 7(a) shows that the most amplified structures in standard resolvent analysis travel faster than their true speeds, whereas in Fig. 7(b), the most amplified structures in eddy resolvent analysis travel slower. Despite the large differences between DNS and the linear analyses, there are two regions in Fig. 7(b) where the discrepancy is small. The first is denoted by the dashed, black rectangle and corresponds to small values of both k_x and k_y, where $c^+ \approx 18.9$. The second is denoted by the solid black rectangle, which contains wavenumber pairs in the range $(k_x, k_y) = (1 \leqslant k_x \leqslant 5, 30 \leqslant k_y \leqslant 34)$ where $c^+ \approx 10$. As will be discussed in the next section, the reasons for why these two wavenumber regions are estimated reasonably well by the eddy resolvent can be related back to the wall-normal profile of the eddy viscosity $\nu_T(z)$.

V. MODE SHAPES AND THE CESS EDDY VISCOSITY PROFILE

The previous section analyzed the linear predictions of the standard and eddy resolvents using scalar quantities such as the low-rank maps, projection coefficients, and maximum wave speeds. This section considers the wall-normal profiles of both mode shapes in Sec. V A and the Cess eddy viscosity profile itself in Sec. V B to predict the agreement between SPOD and resolvent and eddy modes at higher Reynolds numbers.

A. SPOD, resolvent, and eddy modes

The SPOD, resolvent, and eddy mode shapes are compared for four wavenumber triplets that are described in Table II. Mode 0 is a streamwise-constant mode and its most energetic frequency is $\omega = 0$. The other wavenumber pairs are chosen such that modes 1, 2, and 3 have their peak energy around $z = -0.5, z = -0.75$, and $z^+ = 15$, respectively. The maximum wave speed from SPOD is reported as $c^+_{\max,\text{SPOD}}$. Table II reports $c^+_{\max,\text{resolvent}}$ and $c^+_{\max,\text{eddy}}$, the maximum wave speeds identified by

TABLE II. The wavenumber triplets for modes 0–3 along with predictions from resolvent and eddy analysis.

Mode	k_x	k_y	$c_{max,SPOD}^+$	$c_{max,resolvent}^+$	$c_{max,eddy}^+$	γ	γ^e	γ_{95}	γ_{95}^e
0	0	4	$\omega = 0$	$\omega = 0$	$\omega = 0$	0.898	0.978	6	2
1	1	2	18.5	19.0	18.5	0.663	0.956	36	2
2	2	8	16.8	20.5	13.8	0.586	0.877	56	6
3	4	30	10.1	15.3	9.50	0.864	0.950	40	2

resolvent and eddy analysis, respectively. The wave speed selected for plotting purposes, however, is kept fixed at $c_{max,SPOD}^+$. The purpose of comparing $c_{max,SPOD}^+$ and $c_{max,eddy}^+$ is to emphasize that the eddy resolvent produces good predictions when $c_{max,SPOD}^+ \approx c_{max,eddy}^+$. The parameter $c_{max,resolvent}^+$, meanwhile, does not provide information about the quality of predictions from standard resolvent analysis. Finally, Table II quantifies the number of resolvent modes needed such that

$$\sqrt{\sum_{i=1}^{\gamma_{95}} \left(\frac{\langle \hat{\boldsymbol{v}}_1(\boldsymbol{k}), \hat{\boldsymbol{\psi}}_i(\boldsymbol{k}) \rangle}{\|\hat{\boldsymbol{v}}_1(\boldsymbol{k})\| \cdot \|\hat{\boldsymbol{\psi}}_i(\boldsymbol{k})\|} \right)^2} > 0.95, \tag{19a}$$

$$\sqrt{\sum_{i=1}^{\gamma_{95}^e} \left(\frac{\langle \hat{\boldsymbol{v}}_1(\boldsymbol{k}), \hat{\boldsymbol{\psi}}_i^e(\boldsymbol{k}) \rangle}{\|\hat{\boldsymbol{v}}_1(\boldsymbol{k})\| \cdot \|\hat{\boldsymbol{\psi}}_i^e(\boldsymbol{k})\|} \right)^2} > 0.95. \tag{19b}$$

Figure 8 presents the SPOD, resolvent, and eddy mode for mode 0. As indicated in Table II, both the standard and eddy resolvents correctly identify $\omega = 0$ as the most amplified frequency. The projection coefficients γ and γ^e are also large for this choice of $\boldsymbol{k}$. The number of resolvent or eddy modes needed to achieve $\gamma = 0.95$, therefore, is $\gamma_{95} = 6$ and $\gamma_{95}^e = 2$, respectively. The agreement between the resolvent and SPOD modes themselves, however, is not as compelling as $\gamma = 0.898$ might suggest. Although the streamwise velocity component is predicted reasonably well, the spanwise and wall-normal components are significantly underestimated due to the high non-normality of the resolvent operator [43,44]. The eddy resolvent is also non-normal but the addition of eddy viscosity results in a more normal operator [8]. Since the streamwise component is also dominant for the SPOD mode, it has a disproportionate influence on γ thus resulting in a higher value than might be expected from visual inspection of the mode shapes. The agreement between the SPOD and eddy modes, on the other hand, is better for all velocity components, resulting in $\gamma^e = 0.978$.
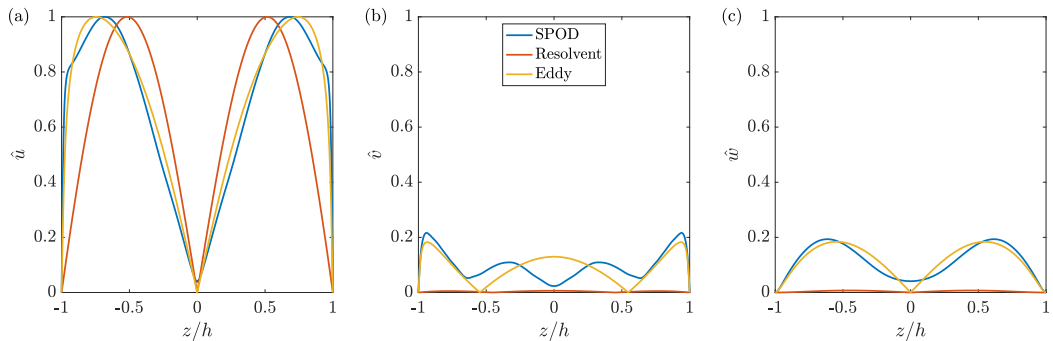

FIG. 8. The (a) streamwise, (b) spanwise, and (c) wall-normal components of the leading SPOD, resolvent, and eddy modes for mode 0 for which $\boldsymbol{k} = (0, 4, \omega = 0)$.
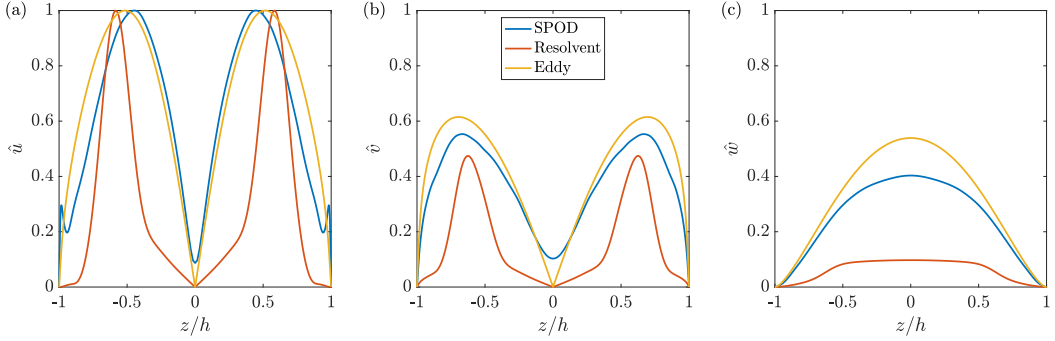
FIG. 9. The (a) streamwise, (b) spanwise, and (c) wall-normal components of the leading SPOD, resolvent, and eddy modes for mode 1 for which $\boldsymbol{k} = (1, 2, 18.5)$.

Mode 1 is an energetic structure in the outer region of the flow with a wavenumber triplet of $\boldsymbol{k} = (1, 2, 18.5)$. Table II shows that $c_{\text{max,SPOD}}^+ = 18.5$ and this is in good agreement with predictions from standard and eddy resolvent analysis. Figure 9 illustrates that while the resolvent modes do not agree well with the SPOD modes, the eddy modes show reasonable agreement with SPOD. This is reflected in the projection coefficients as $\gamma^e = 0.956$ is higher than $\gamma = 0.663$. It also takes significantly fewer eddy modes to reconstruct the leading SPOD mode since $\gamma_{95}^e = 2$ whereas $\gamma_{95} = 36$. It was observed in Refs. [8,13,45] that, when using resolvent modes, many suboptimal modes are needed to reconstruct the velocity field for high-aspect-ratio structures. One reason is that the streamwise and spanwise components of velocity are highly localized in the wall-normal direction due to the critical-layer mechanism [1,13,22,46,47]. The eddy modes, on the other hand, are smoothed out in z by the eddy viscosity. Another factor is that, similar to mode 0, the wall-normal velocity component is underestimated by resolvent analysis as seen in Fig. 9(c). The agreement between the SPOD and eddy modes, meanwhile, is very good for all velocity components and wall-normal locations except the near-wall region of the streamwise component, as seen in Fig. 9(a).

Mode 2 is another structure in the outer region of the flow with a wavenumber triplet of $\boldsymbol{k} = (2, 8, 16.8)$. The streamwise velocity component is most energetic at $z = -0.75$ which is closer to the wall in comparison to $z = -0.5$ for mode 1. Neither standard nor eddy resolvent analysis is capable of predicting the maximum wave speed for mode 2. Consistent with the trends observed in Fig. 7, the standard resolvent predicts a wave speed that is too fast while the eddy resolvent predicts a wave speed that is too slow. As explained earlier, for plotting the resolvent and eddy modes in Fig. 10, $c_{\text{resolvent}}^+$ and c_{eddy}^+ are chosen to be the maximum wave speed as identified by
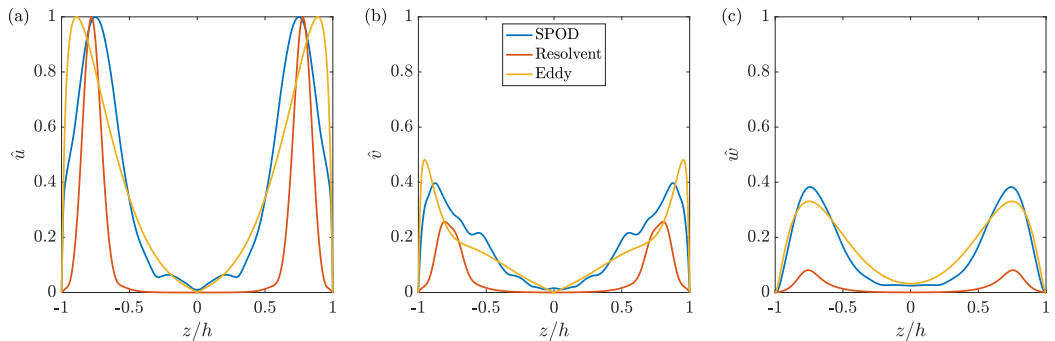

FIG. 10. The (a) streamwise, (b) spanwise, and (c) wall-normal components of the leading SPOD, resolvent, and eddy modes for mode 2 for which $\boldsymbol{k} = (2, 8, 16.8)$.
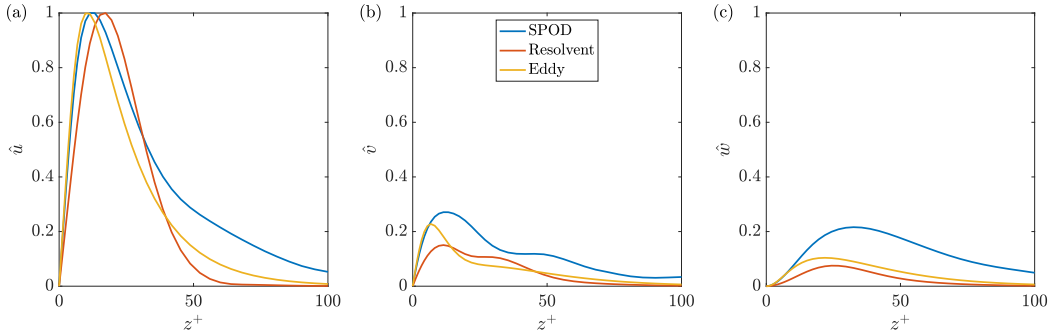
FIG. 11. The (a) streamwise, (b) spanwise, and (c) wall-normal components of the leading SPOD, resolvent, and eddy modes for Mode 3 for which $\boldsymbol{k} = (4, 30, 10.1)$.

SPOD, i.e., $c^+_{\mathrm{max,SPOD}}$. It can be remarked that the projection coefficients belie the true agreement between various mode shapes. When considering the resolvent modes, although $\gamma = 0.586$ seems low, the modes still capture the wall-normal location of the peak streamwise energy reasonably well. However, similar to mode 1, the modes are localized about the critical layer and the wall-normal component is underestimated, resulting in a relatively low γ. The eddy modes appear to be in significantly better agreement as $\gamma^e = 0.877$. Unlike resolvent analysis, however, the wall-normal locations of the peaks in streamwise and spanwise energies of the eddy modes fall below their true locations, a trend that becomes more apparent for higher Reynolds numbers (see Ref. [22]). Even though it is not explicitly shown here for the sake of brevity, for structures with $c^+_{\mathrm{max,eddy}} <$ $c^+_{\mathrm{max,SPOD}}$, the peak streamwise and spanwise energies of the eddy mode are located below the correct wall-normal location identified by SPOD. Mode 2, consequently, is the only wavenumber triplet for which $\gamma^e_{95} = 6$ since suboptimal modes are required to "lift" the structure to its proper height. Fifty-eight modes, meanwhile, are required for resolvent modes to achieve $\gamma = 0.95$.

Figure 11 considers mode 3, which is representative of the near-wall cycle. The agreement between the SPOD and resolvent wave speeds is poor but agreement between the mode shapes is high as $\gamma = 0.864$. Similar to mode 0, the streamwise velocity component is the dominant component for mode 3, thus relegating the influence of the other two velocity components in computing γ. As seen in Table II, the eddy resolvent is close to identifying the most energetic wave speed. Furthermore, the SPOD and eddy mode shapes in Fig. 11 are in very good agreement for the streamwise velocity component and good agreement for the spanwise and wall-normal velocity components, resulting in $\gamma^e = 0.950$. It is clear, furthermore, that eddy modes are a more efficient basis since $\gamma^e_{95} = 2$ compared to $\gamma_{95} = 40$.

### B. Cess eddy viscosity and effective Reynolds number

In this section, the Cess eddy viscosity profile is studied in greater detail in order to predict the agreement between SPOD and resolvent and/or eddy modes at higher Reynolds numbers. The profiles are obtained for a range of Reynolds numbers using Eq. (10). It is particularly interesting to look at the profiles around $z^+ = 15$ and $z = -0.5$ due to the good agreement between SPOD and eddy resolvent analysis for modes 1 and 3 that have their peak energies at these wall heights. In Fig. 12(a), the eddy viscosity profiles are premultiplied by Re_τ, resulting in a collapse near the wall. The profiles for $\mathrm{Re}_\tau = 180$ and $\mathrm{Re}_\tau = 550$ begin to diverge from the other Reynolds numbers around $z^+ = 10$ and $z^+ = 20$, respectively, but the agreement among all profiles is good, particularly around $z^+ = 15$. This wall-normal location is important since it coincides with the location of the structures associated with the near-wall cycle that travel at a wave speed of $c^+ = 10$. It therefore seems reasonable to assume that, for all Reynolds numbers, the eddy resolvent will correctly predict
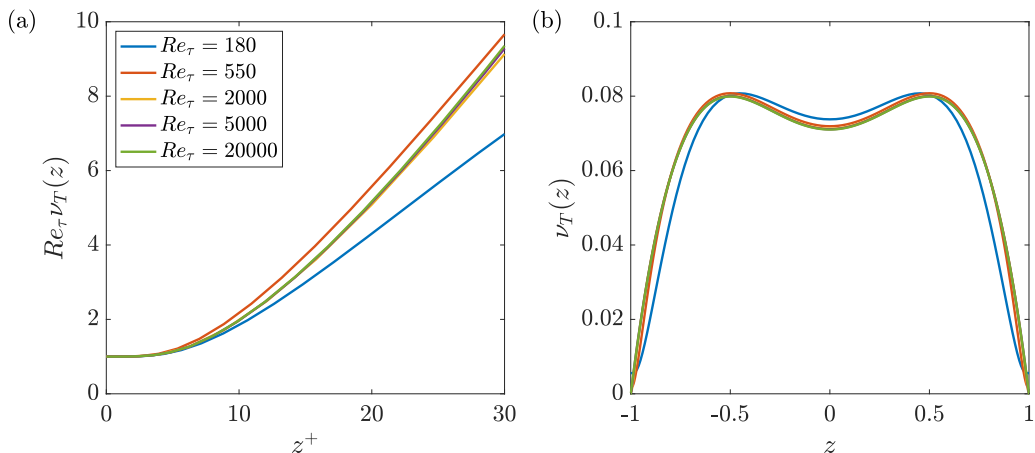
FIG. 12. Wall-normal profiles of (a) $\mathrm{Re}_\tau \nu_T$ and (b) ν_T for various Re_τ.

the structures that are located at these wall heights of $z^+ \approx 15$ and therefore convect at wave speeds around $c^+ = 10$.

In Fig. 12(b), $\nu_T(z)$ is plotted in outer units for Reynolds numbers in the range $180 \leqslant \mathrm{Re}_\tau \leqslant 20\,000$. The profiles for all Reynolds numbers other than $\mathrm{Re}_\tau = 180$ are virtually indistinguishable in the outer region. The largest differences occur near and at the walls where $\nu_T(\pm 1) = \nu$. The maximum value of ν_T is 0.08 and occurs at $z = \pm 0.5$. Mode 1, for which the eddy resolvent gives good predictions, was also found to be most energetic at this wall height of $z = \pm 0.5$. Since ν_T at $z = \pm 0.5$ remains roughly constant with Reynolds number, it can be hypothesized that the eddy mode shapes for wavenumbers with $c_{\max}^+ = U^+(\pm 0.5) \approx U_{\mathrm{CL}}^+ - 2$ are unaffected by Re_τ. This hypothesis is tested in Fig. 13, where the mode shapes of structures with $c_{\max}^+ \approx U_{\mathrm{CL}}^+ - 2$ are compared across different Re_τ. A second hypothesis, which is also tested in Fig. 13, is that the wall-normal-varying eddy viscosity $\nu_T(z)$ can be replaced by a constant eddy viscosity model, i.e., $\nu_T = \mathrm{Re}_T$, where Re_T is the effective Reynolds number. For the case of a turbulent jet, Refs. [14,16,48] showed that a constant eddy viscosity model can improve the agreement between SPOD and eddy modes.

Figure 13 compares the mode shapes for $\boldsymbol{k} = (1, 2, U_{\mathrm{CL}}^+ - 2)$ from standard resolvent analysis, eddy resolvent analysis, and eddy resolvent analysis setting $\mathrm{Re}_T = 1/(\max(\nu_T)) = 12.5$ as done in Ref. [49]. If $\nu_T = \mathrm{Re}_T$, then only the mean profile is affected by changes in Reynolds number.
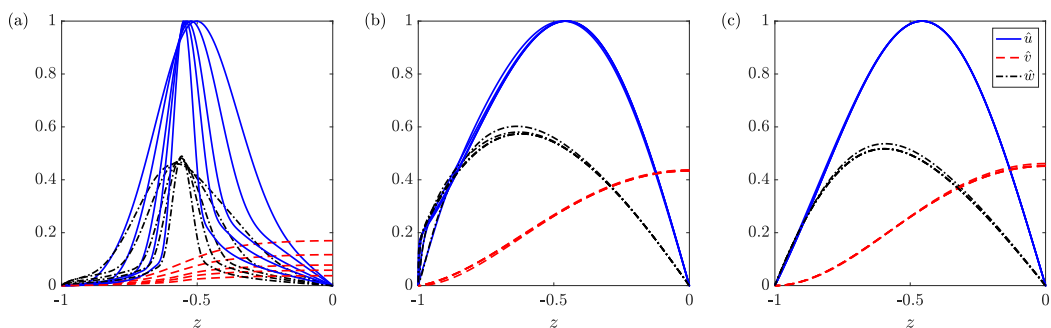
FIG. 13. Mode shapes for $\boldsymbol{k} = (1, 2, U_{\mathrm{CL}}^+ - 2)$ from (a) standard resolvent analysis, (b) eddy resolvent analysis, and (c) eddy resolvent analysis setting $\mathrm{Re}_T = 12.5$. The Reynolds numbers range from $\mathrm{Re}_\tau = 180$ up to $\mathrm{Re}_\tau = 20\,000$.
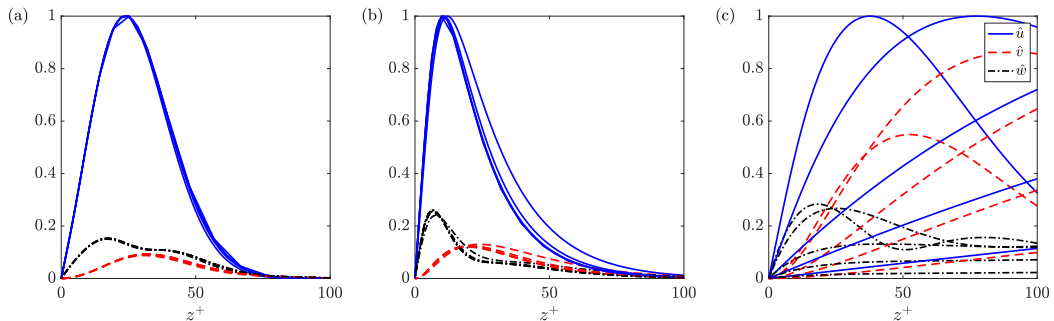
FIG. 14. Mode shapes for $(k_x^+, k_y^+, c^+) = (2\pi/1000, 2\pi/100, 10)$ from (a) standard resolvent analysis, (b) eddy resolvent analysis, and (c) eddy resolvent analysis setting $\mathrm{Re}_T = 12.5$. The Reynolds numbers range from $\mathrm{Re}_\tau = 180$ up to $\mathrm{Re}_\tau = 20\,000$.

All sets of modes are computed for the same Reynolds numbers that appeared in Fig. 12 and are normalized by the maximum value of the streamwise velocity component. The resolvent modes in Fig. 13(a) are influenced heavily by the choice of Re_τ. The streamwise and spanwise velocity components become increasingly localized about the critical layer at $z = -0.5$ as the Reynolds number increases. The shape of the wall-normal component, on the other hand, is roughly constant but its magnitude relative to the wall-parallel velocity components decreases with increasing Reynolds number.

The impact of Reynolds number on the eddy and constant Re_T modes in Figs. 13(b) and 13(c) is negligible. The only difference among the eddy modes in Fig. 13(b) is that for $\mathrm{Re}_\tau = 180$, the streamwise and spanwise velocity components are less attached to the wall in comparison to the other profiles which appear more blunt, i.e., flatter, near the wall. A similar difference emerges between the eddy and constant Re_T modes in that neither the streamwise nor spanwise components exhibit blunt behavior near the wall for any Reynolds number considered. The agreement between eddy and constant Re_T modes, nonetheless, is remarkable given that the constant eddy viscosity model is so simple.

The applicability of the constant eddy viscosity model, however, is limited to scales that have maximum streamwise energy at $z = \pm 0.5$. Figure 14 compares the mode shapes for $(k_x^+, k_y^+, c^+) = (2\pi/1000, 2\pi/100, 10)$, which are representative of the near-wall cycle, from standard resolvent analysis, eddy resolvent analysis, and eddy resolvent analysis setting $\mathrm{Re}_T = 1/(\max(\nu_T)) = 12.5$. The Reynolds number has little impact on the resolvent and eddy modes but has a major impact on the constant Re_T modes. As the Reynolds number increases, the mode shapes become increasingly less localized about the critical layer. The location of the peak energy of all three velocity components, furthermore, gradually shifts closer to the channel centerline and away from the wall. Although it is not shown in the interest of brevity, the same trends can be observed for other values of Re_T. The wall-varying profile of the eddy viscosity near the wall, consequently, is essential to capture the correct mode shapes for wavenumber triplets that are associated with the near-wall cycle.

VI. NONLINEAR ENERGY TRANSFER AND EDDY VISCOSITY

The improved agreement between SPOD and eddy modes indicates that eddy viscosity is able to partially model the effect of $\hat{f}$ for particular scales such as modes 1 and 3. In this section, the energy dissipation and transport that are introduced by the eddy viscosity are examined in greater detail to explain the success or failure of eddy analysis in predicting the correct structures. Section VI A considers the effect of the wall-normal-varying effective Reynolds number $\nu_T(z) - \nu$ and also the eddy viscosity gradient $\nu_T' = d\nu_T/dz$. In Sec. VI B, the dissipation and transport are examined across wall heights in order to determine how they affect the eddy mode shapes. It is demonstrated in

Sec. VI C that artificially adjusting the eddy viscosity gradient can significantly manipulate the eddy mode shapes, particularly in the near-wall region. Section VI D discusses the types of interactions that are modeled by the eddy viscosity.

A. Eddy dissipation and transport

As explained in Ref. [8], the addition of eddy viscosity introduces new dissipation and transport terms into the kinetic energy balance for each scale. These terms can be derived by expanding the viscous term in Eq. (9) and Fourier-transforming in the homogeneous directions

$$\nabla \cdot [\nu_T (\nabla \hat{\boldsymbol{u}} + \nabla \hat{\boldsymbol{u}}^T)] = \nu_T \nabla^2 \hat{\boldsymbol{u}} + (\nabla \cdot \nu_T)(\nabla \hat{\boldsymbol{u}} + \nabla \hat{\boldsymbol{u}}^T), \tag{20}$$

where factors of $1/\mathrm{Re}_\tau$ and $1/\nu$ have been ignored to simplify the analysis. Rewriting Eq. (20) in index notation, taking the inner product with respect to u_i, averaging the final expression in time, and then isolating the contribution of the eddy viscosity gives the additional dissipation and transport terms introduced by eddy viscosity as

$$\widehat{Edd}(k_x, k_y, z)$$

$$= \underbrace{-\nu_t(z)\overline{\frac{\partial \hat{u}_i}{\partial x_j}\left(\frac{\partial \hat{u}_i^*}{\partial x_j} + \frac{\partial \hat{u}_j^*}{\partial x_i}\right)}}_{\hat{D}(k_x, k_y, z)} + \underbrace{\nu_t(z)\overline{\frac{\partial}{\partial x_j}\left[\hat{u}_i\left(\frac{\partial \hat{u}_i^*}{\partial x_j} + \frac{\partial \hat{u}_j^*}{\partial x_i}\right)\right]}}_{\hat{V}(k_x, k_y, z)} + \underbrace{\frac{d\nu_t(z)}{dz}\overline{\hat{u}_i\left(\frac{\partial \hat{u}_i^*}{\partial z} + \frac{\partial \hat{w}^*}{\partial x_i}\right)}}_{\hat{G}(k_x, k_y, z)}, \tag{21}$$

where $i, j = 1, 2, 3$ and $\nu_t = \nu_T - \nu$. The term $\hat{D}$ is the dissipation due to eddy viscosity and this term is guaranteed to be negative at all wall-normal locations. $\hat{V} + \hat{G}$ is transport introduced by the eddy viscosity, with $\hat{V}$ the transport due to the wall-normal profile of ν_t and $\hat{G}$ the transport due to the wall-normal gradient of eddy viscosity, $d\nu_t/dz$. The combined effect of eddy viscosity is $\widehat{Edd} = \hat{D} + \hat{V} + \hat{G}$ and, without eddy viscosity, $\widehat{Edd} = 0$.

B. Positive and negative energy transfers

It is guaranteed that $\hat{D}$ is real and negative at all wall-normal locations, but this is not the case for the transport term $\hat{V}$ and $\hat{G}$ since $\hat{V} + \hat{G}$ has to integrate to zero over the wall-normal direction. For instance, it can be shown that $\hat{G}$ is likely to be positive near the wall. If the final term of Eq. (21) is expanded in full, then $\hat{G}$ becomes

$$\hat{G} = \frac{d\nu_t}{dz}\overline{\hat{u}\frac{\partial \hat{u}}{\partial z}} + \frac{d\nu_t}{dz}\overline{\hat{v}\frac{\partial \hat{v}}{\partial z}} + 2\frac{d\nu_t}{dz}\overline{\hat{w}\frac{\partial \hat{w}}{\partial z}} + \frac{d\nu_t}{dz}\overline{\hat{u}\frac{\partial \hat{w}}{\partial x}} + \frac{d\nu_t}{dz}\overline{\hat{v}\frac{\partial \hat{w}}{\partial y}}. \tag{22}$$

Assuming that the streamwise velocity component is significantly stronger than the spanwise and wall-normal components, i.e., $\hat{u} \gg \hat{v}, \hat{w}$, then Eq. (22) can be approximated as

$$\hat{G} \approx \frac{d\nu_t}{dz}\overline{\hat{u}\frac{\partial \hat{u}}{\partial z}}. \tag{23}$$

For the lower wall, $\hat{u} = 0$ due to the no-slip condition and both $\hat{u}$ and $\frac{\partial \hat{u}}{\partial z}$ must be either both positive or negative moving away from the wall. In either case, the product of $\hat{u}$ and $\frac{\partial \hat{u}}{\partial z}$ is positive. As shown in Fig. 15, $\frac{d\nu_t}{dz} > 0$ near the lower wall so the product of all three terms that appear in Eq. (23) is positive in the near-wall region. Although several approximations have been made to arrive at this result, it is significant because $\hat{V}$ and $\hat{G}$ attempt to model nonlinear transport processes. If $\hat{V}$ or $\hat{G}$ can have significant positive values near the wall as implied here, then it would imply that eddy viscosity models significant energy transport towards the wall. It is then important to understand how this transport towards the wall compares to DNS.

Before examining profiles of $\hat{D}(z)$, $\hat{V}(z)$, and $\hat{G}(z)$ for specific scales, it is worth commenting further on the eddy viscosity gradient profiles in Fig. 15. Similar to the ν_T profiles in Fig. 12, it can
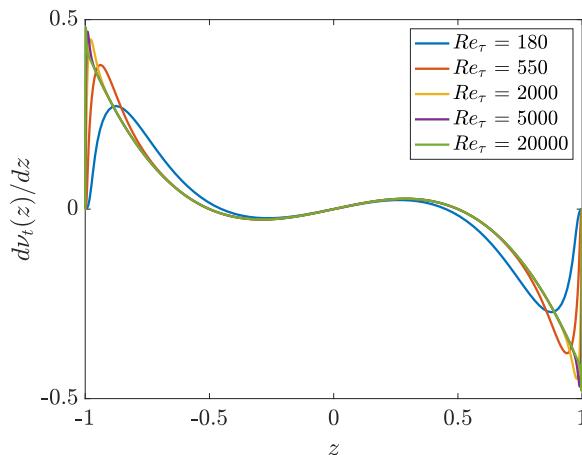
FIG. 15. Wall-normal profiles of the eddy viscosity gradient ν_t' for various Re_τ.

be observed that Re_τ has a negligible impact on ν_t' for most wall-normal locations. The maxima and minima of profiles become more extreme and closer to the wall as Re_τ increases. This localization suggests that $\hat{G}(z)$ is likely to be more concentrated in the near-wall regions and have a larger magnitude for higher Reynolds numbers.

Figure 16(a) compares $\hat{Q}(z) = -\widehat{\hat{u}_i \frac{\partial}{\partial x_j} \widehat{u_i u_j}}$, the time-averaged nonlinear transfer from DNS, for $(k_x, k_y) = (0, 4)$ with $\widehat{Edd}(z)$ in Fig. 16(b). Since the DNS results are averaged in time, they include contributions from all frequencies (wave speeds), whereas the eddy predictions are for the most energetic frequency only. This is a reasonable approximation since $\omega = 0$ dominates over all other frequencies (recall that wave speed is ill defined for $k_x = 0$ modes). There is good agreement between $\hat{Q}(z)$ and $\widehat{Edd}(z)$ at nearly all wall-normal locations other than the near-wall region. In the region very close to the wall $\widehat{Edd}(z)$ correctly predicts positive energy transfer, but its magnitude is too large. In Fig. 16(c), $\widehat{Edd}(z)$ is split into the contributions from $\hat{D}(z)$, $\hat{V}(z)$, and $\hat{G}(z)$. From Fig. 16(c) we see that $\hat{G}(z)$ is responsible for the positive contributions to $\widehat{Edd}(z)$, as predicted by Eq. (23), and that $\hat{D}(z)$ and $\hat{V}(z)$ account for the bulk of the negative contributions. Close to the wall $\hat{V}(z)$ does have a positive contribution towards $\widehat{Edd}(z)$; however, this contribution is insignificant in comparison to $\hat{G}(z)$.
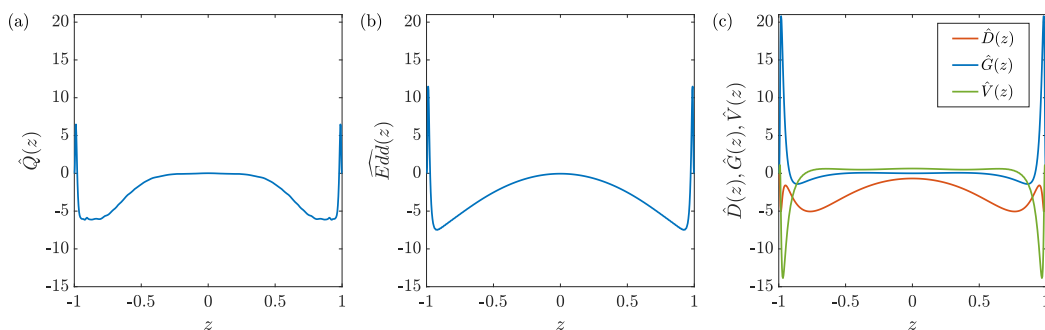
FIG. 16. (a) Time-averaged nonlinear transfer from DNS for $(k_x, k_y) = (0, 4)$ compared to (b) $\widehat{Edd}(z)$ and (c) its components for $\omega = 0$.
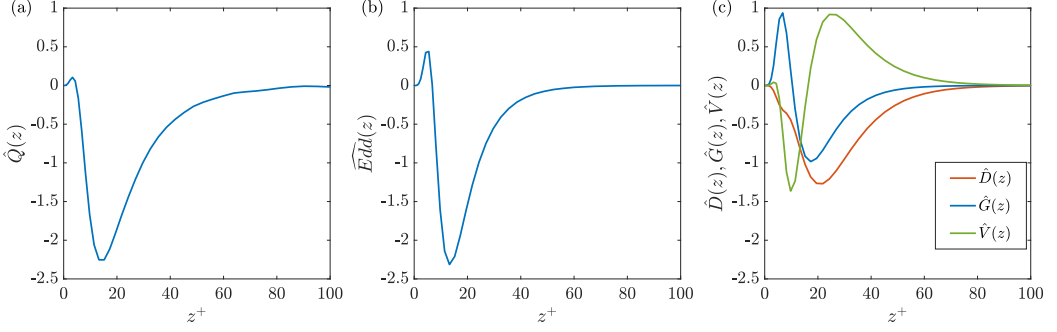
FIG. 17. (a) Time-averaged nonlinear transfer from DNS for $(k_x, k_y) = (4, 30)$ compared to (b) $\widehat{Edd}(z)$ and (c) its components for $c^+ = 10$.

Figure 17(a) compares $\hat{Q}(z)$ for $(k_x, k_y) = (4, 30)$ with $\widehat{Edd}(z)$ in Fig. 17(b). The eddy predictions are for the most energetic wave speed $c^+ = 10$. Good agreement can be observed between $\hat{Q}(z)$ and $\widehat{Edd}(z)$ although $\widehat{Edd}(z)$ is most negative at $z^+ = 20$ instead of $z^+ = 15$. Similar to the previous scale considered in Fig. 16, $\widehat{Edd}(z)$ overestimates the positive energy transfer in the near-wall region which, as seen in Fig. 17(c), is mainly driven by $\hat{G}(z)$.

It can be concluded that the eddy viscosity gradient plays an important role in modeling positive energy transfer processes. The predicted $\widehat{Edd}(z)$, nonetheless, exceeds the true nonlinear transfer in the near-wall region. The next section considers the effect of artificially weakening the eddy viscosity gradient to analyze its impact on the resulting mode shapes.

C. Artificially adjusting the eddy viscosity gradient

In this section, the strength of the eddy viscosity term is altered by introducing a scaling factor $\mathcal{G}$ such that Eq. (20) becomes

$$\nabla \cdot [\nu_T (\nabla \hat{\boldsymbol{u}} + \nabla \hat{\boldsymbol{u}}^T)] = \nu_T \nabla^2 \hat{\boldsymbol{u}} + \mathcal{G}(\nabla \cdot \nu_T)(\nabla \hat{\boldsymbol{u}} + \nabla \hat{\boldsymbol{u}}^T), \tag{24}$$

where $\mathcal{G} \geqslant 0$ controls the strength of the eddy viscosity gradient term. Figure 18 illustrates the impact of artificially adjusting $\mathcal{G}$ for mode 0. It can be seen that as $\mathcal{G}$ increases, the peak energy of the streamwise and spanwise velocity components shifts closer to the wall. The shape of the wall-normal velocity component is less affected but its magnitude decreases. It can be reasoned that increasing $\mathcal{G}$ results in greater positive energy transfer in the near-wall region. The energy of the modes, consequently, is redistributed towards the wall and to the wall-parallel velocity components. For some scales, $\mathcal{G}$ is too strong, resulting in too much energy in the streamwise and spanwise
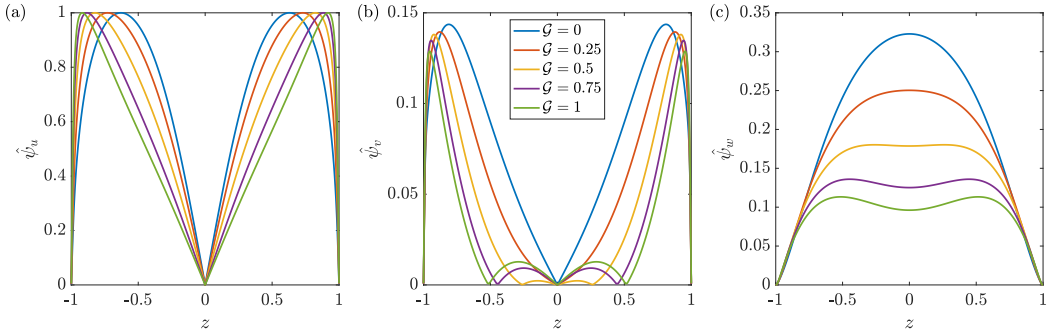

FIG. 18. Leading eddy modes for $\boldsymbol{k} = (0, 4, 0)$ for various strengths of the eddy viscosity gradient $\mathcal{G}$.
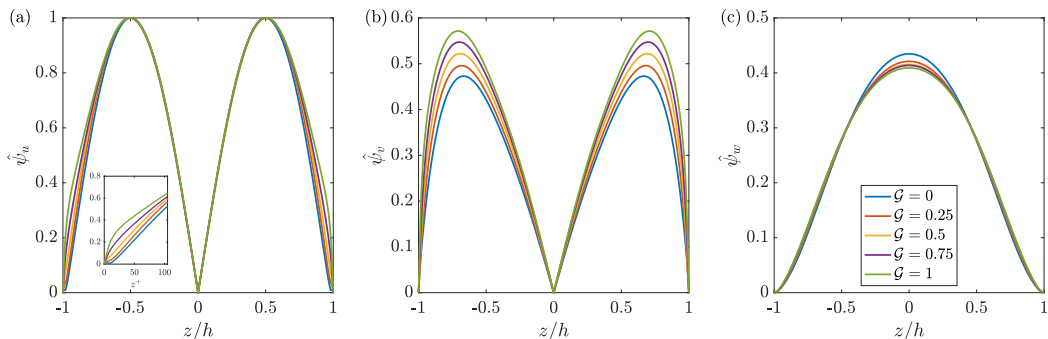
FIG. 19. Leading eddy modes for $k = (1, 2, 18.5)$ for various strengths of the eddy viscosity gradient $\mathcal{G}$.

velocity components near the wall as seen for mode 2 in Sec. V A. These biased mode shapes explain why linear-based estimation techniques that use an eddy viscosity model, e.g., Refs. [41,46], overpredict the strength of fluctuations in the near-wall region when measurements are known in the logarithmic region. The biased mode shapes are also consistent with Ref. [21], which found that the eddy viscosity model underestimates fluctuations when using wall-based measurements.

Figure 19 presents the effect of $\mathcal{G}$ on the mode 1 shapes. Unlike mode 0, $\mathcal{G}$ has almost no impact on the structures although the spanwise component becomes slightly less energetic relative to the other velocity components as $\mathcal{G}$ increases. The main difference occurs in the streamwise velocity component very close to the wall. The inset of Fig. 18 shows that the mode shape becomes flatter or more blunt as $\mathcal{G}$ increases. Similar to mode 0, the flatter profiles can be attributed to $\hat{G}$ injecting energy in this region of the flow. This also explains why the constant eddy viscosity model, which has a wall-normal gradient of zero everywhere, was not able to reproduce the near-wall behavior in Fig. 13(c) that appeared in Fig. 13(b).

D. Discussion

The previous sections have analyzed the energy transfer processes that can be modeled by the Cess eddy viscosity profile. This section aims to contextualize these results with respect to recent low-order modeling efforts in the literature. One key challenge is to identify the smallest subset of nonlinear interactions that are needed to sustain a wall-bounded turbulent flow at high Reynolds numbers. The generalized quasilinear (GQL) approximation [50], in particular, is able to reproduce key statistical features of wall-bounded turbulence [30]. The GQL approximation decomposes the flow into a low-wavenumber group and a high-wavenumber group. Nonlinear interactions involving the high-wavenumber group are removed. If the low-wavenumber group is restricted to the mean flow, the quasilinear approximation (QLA) is recovered [51–54].

Reference [30] has shown that the GQL approach retains triadic interactions that are responsible for the scattering mechanism and inverse energy transfer in the near-wall region. The former can be attributed to low-high wavenumber interactions that feed into high wavenumbers while the latter arise from high-high wavenumber interactions that feed into low wavenumbers. It is posited that the negative energy transfer modeled by eddy viscosity through $\hat{D}$ can be interpreted as a scattering mechanism that removes energy from larger scales and redistributes it to smaller scales. The positive energy transfer introduced by $\hat{G}$, on the other hand, models the inverse energy transfer in the near-wall region. The combined effect of these two transfers, therefore, encapsulates the effect of small scales on the large scales.

VII. CONCLUSIONS

The predictions of resolvent analysis with and without eddy viscosity have been evaluated for a friction Reynolds number of $\text{Re}_\tau = 550$. The eddy resolvent predicted better the low-rank

behavior of SPOD modes in comparison to the standard resolvent. The low-rank map of the standard resolvent, however, was able to predict well the turbulent kinetic energy spectrum. In all other metrics, nonetheless, predictions from the eddy resolvent agreed better with DNS over the standard resolvent. The highest projection coefficients were obtained for eddy modes with wave speeds of $c^+ = 10$ and $c^+ = 18.9$. These correspond to structures associated with the near-wall cycle and structures that are most energetic at $z = \pm 0.5$. The maximum wave speed identified by the eddy resolvent was also found to match that of DNS for these two types of structures. For most wavenumber pairs, however, both standard and eddy resolvent analysis failed to predict the maximum wave speed. Resolvent analysis overestimated the correct wave speed while eddy analysis underestimated the correct wave speed.

The importance of wave speed on the projection coefficients motivated the selection of specific scales for comparing the SPOD modes to the resolvent and eddy modes. Consistent with previous studies, resolvent modes tended to be localized around the critical layer [1] and the streamwise velocity component was too strong relative to the spanwise and wall-normal velocity components. All three velocity components of the eddy modes, meanwhile, matched their SPOD counterparts for the wave speeds of $c^+ = 10$ and $c^+ = 18.9$. For other wave speeds, eddy resolvent analysis predicted structures that were energetic closer to the wall than the SPOD modes. It was concluded that for higher Reynolds numbers, SPOD and eddy modes will agree for $c^+ = 10$ and $c^+ = U_{\text{CL}}^+ - 2$ due to the invariance of the Cess profile in the near-wall region up to $z^+ = 15$, when it is premultiplied by Re_τ, and in the outer region where it is maximum at $z = \pm 0.5$. Modes for $c^+ = U_{\text{CL}}^+ - 2$ could also be obtained with reasonable accuracy by setting $\nu_T = \text{Re}_T = 12.5$.

Finally, there was an investigation into the energy dissipation and transport terms that are modeled by the Cess profile. The eddy dissipation acts as an effective Reynolds number that varies spatially. Similar to dissipation, this effective Reynolds number term is guaranteed to be real and negative. The eddy transport term, on the other hand, has two contributions: one that originates from the wall-normal profile of eddy viscosity and the second that originates from the wall-normal gradient of the eddy viscosity. This term that originates from the eddy viscosity gradient tends to be positive in the near-wall region. The combined effect of these energy transfer processes models well the actual nonlinear transfer taking place in DNS, although the positive energy transfer near the wall is overestimated. This explains the tendency for eddy modes to be too energetic near the wall.

In order to further improve predictions from resolvent analysis, the Cess profile could be replaced with a scale-dependent eddy viscosity. Reference [16], for example, solved an inverse problem to find the eddy viscosity profile that maximized the projection of the leading resolvent mode onto the leading SPOD mode. The drawback of this approach is that it requires sufficient data in order to compute the leading SPOD mode. As such, other approaches have modified the Cess profile for individual scales using scaling arguments [41] or a stochastic approach to model background turbulence that can inject or dissipate energy of coherent waves [26,55]. Regardless of the approach selected, the Cess profile provides a good initial condition for optimizing an eddy viscosity [56] or modeling the effect of nonlinear terms [57] which can improve estimating turbulent channel flows using resolvent analysis.

APPENDIX A: LINEAR OPERATORS

After elimination of the pressure, the linearized Navier-Stokes equations can be rewritten for the wall-normal velocity $\hat{w}$ and wall-normal vorticity $\hat{\eta} = ik_y\hat{u} - ik_x\hat{v}$. The matrices $\boldsymbol{A}$, $\boldsymbol{B}$, and $\boldsymbol{C}$ that
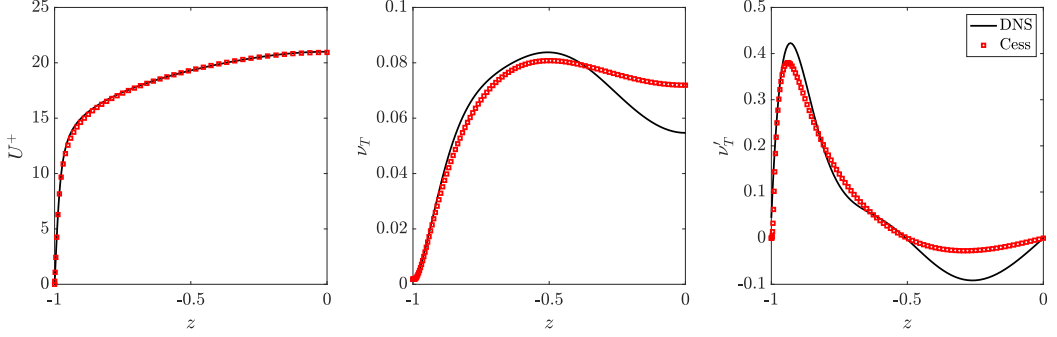
FIG. 20. Comparison of the mean velocity, eddy viscosity, and wall-normal of the eddy viscosity profiles from DNS to the Cess profiles.

appear in Eq. (4) are

$$A = M \begin{bmatrix} \mathcal{L}_{\text{OS}} & 0 \\ -ik_y U' & \mathcal{L}_{\text{SQ}} \end{bmatrix}, \tag{A1a}$$

$$B = M \begin{bmatrix} -ik_x \mathcal{D} & -ik_y \mathcal{D} & -k^2 \\ ik_y & -ik_x & 0 \end{bmatrix}, \tag{A1b}$$

$$C = \frac{1}{k^2} \begin{bmatrix} ik_x \mathcal{D} & -ik_y \\ ik_y \mathcal{D} & ik_x \\ k^2 & 0 \end{bmatrix}. \tag{A1c}$$

The boundary conditions are enforced on both walls as $\hat{w}(\pm 1) = \partial \hat{w}(\pm 1)/\partial z = \hat{\eta}(\pm 1) = 0$. Both $\mathcal{D}$ and $'$ represent differentiation in the wall-normal direction and $k^2 = k_x^2 + k_y^2$. The mass matrix M is defined as

$$M(k_x, k_y) = \begin{bmatrix} \Delta^{-1} & 0 \\ 0 & I \end{bmatrix}, \tag{A2}$$

where $\Delta = \mathcal{D}^2 - k^2$ and I is the identity matrix. The Orr-Sommerfeld $\mathcal{L}_{\text{OS}}$ and Squire $\mathcal{L}_{\text{SQ}}$ operators (Refs. [11,58]) are

$$\mathcal{L}_{\text{OS}} = -ik_x U \Delta + ik_x U'' + (1/\text{Re}_\tau) \Delta^2, \tag{A3a}$$

$$\mathcal{L}_{\text{SQ}} = -ik_x U + (1/\text{Re}_\tau) \Delta. \tag{A3b}$$

With the addition of eddy viscosity, they become

$$\mathcal{L}_{\text{OS}} = -ik_x U \Delta + ik_x U'' + v_T \Delta^2 + 2v_T' \mathcal{D} \Delta + v_T''(\mathcal{D}^2 + k^2), \tag{A4a}$$

$$\mathcal{L}_{\text{SQ}} = -ik_x U + v_T \Delta + v_T' \mathcal{D}. \tag{A4b}$$

APPENDIX B: DNS EDDY VISCOSITY PROFILE

In addition to the Cess eddy viscosity profile, it is possible to compute v_T directly from the DNS mean profile using [59]

$$v_T = -\frac{z}{dU^+/dz}. \tag{B1}$$

The values of dU^+/dz near the center of the channel approach zero so a 12th-order polynomial is fit to the v_T computed from Eq. (B1) in order to obtain a smooth profile.

The mean profile obtained by integrating Eq. (B1) with the Cess eddy viscosity is compared to the DNS mean velocity profile in Fig. 20. Very good agreement can be observed between the two
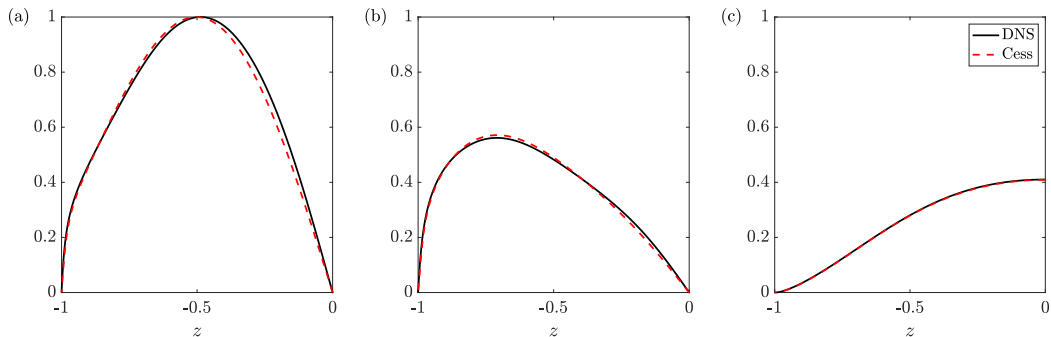
FIG. 21. Comparison of the first eddy resolvent modes using the DNS and Cess eddy viscosity profiles for mode 1.

profiles. The Cess eddy viscosity profile and its wall-normal gradient are compared to the profiles computed from the DNS mean profile in Figs. 20(b) and 20(c), respectively. There is good agreement overall between the two sets of profiles. The Cess and DNS eddy viscosity profiles diverge in the center of the channel. The wall-normal gradients of the profiles also diverge near the center of the channel and near the local maximum at $z = -0.9$.

Despite these differences, the choice of eddy viscosity (Cess or DNS) has a negligible impact on the resulting resolvent modes. Figure 21 compares the resolvent modes for mode 1, which is most likely to be impacted by the differences between the profiles. It can be seen that the resolvent modes are nearly identical. It can be concluded that the resolvent modes are not very sensitive to the choice of eddy viscosity profile as long as the maximum of ν_T and its wall-normal gradient are approximated reasonably well.

---

[1] B. J. McKeon and A. S. Sharma, A critical layer framework for turbulent pipe flow, J. Fluid Mech. **658**, 336 (2010).

[2] A. S. Sharma, R. Moarref, B. J. McKeon, J. S. Park, M. D. Graham, and A. P. Willis, Low-dimensional representations of exact coherent states of the Navier-Stokes equations from the resolvent model of wall turbulence, Phys. Rev. E **93**, 021102(R) (2016).

[3] R. Moarref, A. S. Sharma, J. A. Tropp, and B. J. McKeon, Model-based scaling of the streamwise energy density in high-Reynolds-number turbulent channels, J. Fluid Mech. **734**, 275 (2013).

[4] N. Skouloudis and Y. Hwang, Scaling of turbulence intensities up to $Re_\tau = 10^6$ with a resolvent-based quasilinear approximation, Phys. Rev. Fluids **6**, 034602 (2021).

[5] M. Luhar, A. S. Sharma, and B. J. McKeon, Opposition control within the resolvent analysis framework, J. Fluid Mech. **749**, 597 (2014).

[6] S. Nakashima, K. Fukagata, and M. Luhar, Assessment of suboptimal control for turbulent skin friction reduction via resolvent analysis, J. Fluid Mech. **828**, 496 (2017).

[7] S. S. Toedtli, M. Luhar, and B. J. McKeon, Predicting the response of turbulent channel flow to varying-phase opposition control: Resolvent analysis as a tool for flow control design, Phys. Rev. Fluids **4**, 073905 (2019).

[8] S. Symon, S. J. Illingworth, and I. Marusic, Energy transfer in turbulent channel flows and implications for resolvent modelling, J. Fluid Mech. **911**, A3 (2021).

[9] B. Jin, S. Symon, and S. J. Illingworth, Energy transfer mechanisms and resolvent analysis in the cylinder wake, Phys. Rev. Fluids **6**, 024702 (2021).

[10] W. C. Reynolds and A. K. M. F. Hussain, The mechanics of an organized wave in turbulent shear flow. Part 3. Theoretical models and comparisons with experiments, J. Fluid Mech. **54**, 263 (1972).

[11] G. Pujals, M. García-Villalba, C. Cossu, and S. Depardon, A note on optimal transient growth in turbulent channel flows, Phys. Fluids **21**, 015109 (2009).

[12] Y. Hwang and C. Cossu, Linear non-normal energy amplification of harmonic and stochastic forcing in the turbulent channel flow, J. Fluid Mech. **664**, 51 (2010).

[13] P. Morra, O. Semeraro, D. S. Henningson, and C. Cossu, On the relevance of Reynolds stresses in resolvent analysis of turbulent wall-bounded flows, J. Fluid Mech. **867**, 969 (2019).

[14] P. Kuhn, J. Soria, and K. Oberleithner, Linear modelling of self-similar jet turbulence, J. Fluid Mech. **919**, A7 (2021).

[15] P. Morra, P. A. S. Nogueira, A. V. G. Cavalieri, and D. S. Henningson, The colour of forcing statistics in resolvent analyses of turbulent channel flows, J. Fluid Mech. **907**, A24 (2021).

[16] E. Pickering, G. Rigas, O. T. Schmidt, D. Sipp, and T. Colonius, Optimal eddy viscosity for resolvent-based models of coherent structures in turbulent jets, J. Fluid Mech. **917**, A29 (2021).

[17] J. L. Lumley, *Stochastic Tools in Turbulence* (Academic Press, New York, 1967)

[18] C. Picard and J. Delville, Pressure velocity coupling in a subsonic round jet, Int. J. Heat Fluid Flow **21**, 359 (2000).

[19] A. Towne, O. T. Schmidt, and T. Colonius, Spectral proper orthogonal decomposition and its relationship to dynamic mode decomposition and resolvent analysis, J. Fluid Mech. **847**, 821 (2018).

[20] P. A. S. Nogueira, P. Morra, E. Martini, A. V. G. Cavalieri, and D. S. Henningson, Forcing statistics in resolvent analysis: Application in minimal turbulent Couette flow, J. Fluid Mech. **908**, A32 (2021).

[21] F. R. Amaral, A. V. G. Cavalieri, E. Martini, P. Jordan, and A. Towne, Resolvent-based estimation of turbulent channel flow using wall measurements, J. Fluid Mech. **927**, A17 (2021).

[22] S. Symon, S. J. Illingworth, and I. Marusic, Large-scale structures predicted by linear models of wall-bounded turbulence, J. Phys.: Conf. Ser. **1522**, 012006 (2020).

[23] L. I. Abreu, A. V. G. Cavalieri, P. Schlatter, R. Vinuesa, and D. S. Henningson, Spectral proper orthogonal decomposition and resolvent analysis of near-wall coherent structures in turbulent pipe flows, J. Fluid Mech. **900**, A11 (2020).

[24] T. Ellingsen and E. Palm, Stability of linear flow, Phys. Fluids **18**, 487 (1975).

[25] M. T. Landahl, A note on an algebraic instability of inviscid parallel shear flows, J. Fluid Mech. **98**, 243 (1980).

[26] G. Tissot, A. V. G. Cavalieri, and E. Mémin, Stochastic linear modes in a turbulent channel flow, J. Fluid Mech. **912**, A51 (2021).

[27] M. Lee and R. D. Moser, Spectral analysis of the budget equation in turbulent channel flows at high Reynolds numbers, J. Fluid Mech. **860**, 886 (2019).

[28] T. Kawata and T. Tsukahara, Scale interactions in turbulent plane Couette flows in minimal domains, J. Fluid Mech. **911**, A55 (2021).

[29] P. Doohan, A. P. Willis, and Y. Hwang, Minimal multi-scale dynamics of near-wall turbulence, J. Fluid Mech. **913**, A8 (2021).

[30] C. G. Hernández, Q. Yang, and Y. Hwang, Generalised quasilinear approximations of turbulent channel flow: Part 2. Spanwise scale interactions, J. Fluid Mech. **944**, A34 (2022).

[31] M. R. Jovanović and B. Bamieh, Componentwise energy amplification in channel flows, J. Fluid Mech. **534**, 145 (2005).

[32] J. A. Weideman and S. C. Reddy, A MATLAB differentiation matrix suite, ACM Trans. Math. Softw. **26**, 465 (2000).

[33] B. Barthel, X. Zhu, and B. J. McKeon, Closing the loop: Nonlinear Taylor vortex flow through the lens of resolvent analysis, J. Fluid Mech. **924**, A9 (2021).

[34] W. C. Reynolds and W. G. Tiederman, Stability of turbulent channel flow, with application to Malkus's theory, J. Fluid Mech. **27**, 253 (1967).

[35] R. D. Cess, A survey of the literature on heat transfer in turbulent tube flow, Technical Report No. 8-0529-R24, 1958 (unpublished).

[36] J. C. del Álamo and J. Jiménez, Linear energy amplification in turbulent channels, J. Fluid Mech. **640**, 5 (2009).

[37] P. Welch, The use of fast Fourier transform for the estimation of power spectra: A method based on time averaging over short, modified periodograms, IEEE Trans. Audio Electroacoust. **15**, 70 (1967).

[38] J. F. Gibson, F. Reetz, S. Azimi, A. Ferraro, T. Kreilos, H. Schrobsdorff, M. Farano, A. F. Yesil, S. S. Schütz, M. Culpo, and T. M. Schneider, CHANNELFLOW 2.0 (unpublished).

[39] M. Lee and R. D. Moser, Direct numerical simulation of turbulent channel flow up to Re$_\tau \approx 5200$, J. Fluid Mech. **774**, 395 (2015).

[40] S. D. Muralidhar, B. Podvin, L. Mathelin, and Y. Fraigneau, Spatio-temporal proper orthogonal decomposition of turbulent channel flow, J. Fluid Mech. **864**, 614 (2019).

[41] V. Gupta, A. Madhusudanan, M. Wan, S. J. Illingworth, and M. P. Juniper, Linear-model-based estimation in wall turbulence: Improved stochastic forcing and eddy viscosity terms, J. Fluid Mech. **925**, A18 (2021).

[42] Y. Hwang, Statistical structure of self-sustaining attached eddies in turbulent channel flow, J. Fluid Mech. **767**, 254 (2015).

[43] L. N. Trefethen, A. E. Trefethen, S. C. Reddy, and T. A. Driscoll, Hydrodynamic stability without eigenvalues, Science **261**, 578 (1993).

[44] P. J. Schmid and D. S. Henningson, *Stability and Transition in Shear Flows* (Springer, Berlin, 2001).

[45] K. Rosenberg and B. J. McKeon, Efficient representation of exact coherent states of the Navier-Stokes equations using resolvent analysis, Fluid Dyn. Res. **51**, 011401 (2019).

[46] A. Madhusudanan, S. J. Illingworth, and I. Marusic, Coherent large-scale structures from the linearized Navier-Stokes equations, J. Fluid Mech. **873**, 89 (2019).

[47] S. B. Vadarevu, S. Symon, S. J. Illingworth, and I. Marusic, Coherent structures in the linearized impulse response of turbulent channel flow, J. Fluid Mech. **863**, 1190 (2019).

[48] P. Kuhn, J. S. Müller, S. Knechtel, J. Soria, and K. Oberleithner, Influence of eddy viscosity on linear modeling of self-similar coherent structures in the jet far field, AIAA Scitech 2022 Forum, 2022-0460 (2022).

[49] Y. Hwang, Mesolayer of attached eddies in turbulent channel flow, Phys. Rev. Fluids **1**, 064401 (2016).

[50] J. B. Marston, G. P. Chini, and S. M. Tobias, Generalized Quasilinear Approximation: Application to Zonal Jets, Phys. Rev. Lett. **116**, 214501 (2016).

[51] B. F. Farrell and P. J. Ioannou, Structure and spacing of jets in barotropic turbulence, J. Atmos. Sci. **64**, 3652 (2007).

[52] J. B. Marston, E. Conover, and T. Schneider, Statistics of an unstable barotropic jet from a cumulant expansion, J. Atmos. Sci. **65**, 1955 (2008).

[53] V. L. Thomas, B. K. Lieu, M. R. Jovanović, B. F. Farrell, P. J. Ioannou, and D. F. Gayme, Self-sustaining turbulence in a restricted nonlinear model of plane Couette flow, Phys. Fluids **26**, 105112 (2014).

[54] V. L. Thomas, B. F. Farrell, P. J. Ioannou, and D. F. Gayme, A minimal model of self-sustaining turbulence, Phys. Fluids **27**, 105104 (2015).

[55] G. Tissot, A. V. G. Cavalieri, and E. Mémin, Input-output analysis of the stochastic Navier-Stokes equations: Application to turbulent channel flow, Phys. Rev. Fluids **8**, 033904 (2023).

[56] S Abootorabi and A. Zare, Model-based spectral coherence analysis for high-Reynolds-number turbulent shear flows, J. Fluid Mech. **958**, A16 (2023).

[57] A. Zare, M. R. Jovanović, and T. T. Georgiou, Colour of turbulence, J. Fluid Mech. **812**, 636 (2017).

[58] C. Cossu, G. Pujals, and S. Depardon, Optimal transient growth and very large scale structures in turbulent boundary layers, J. Fluid Mech. **619**, 79 (2009).

[59] H. Tennekes and J. L. Lumley, *A First Course in Turbulence* (MIT Press, Cambridge, MA, 1972).